Fam49/CYRI interacts with Rac1 and locally suppresses protrusions

Loic Fort[1,2*], José Miguel Batista[1,2*], Peter A. Thomason[1], Heather J. Spence[1], Jamie A. Whitelaw[1], Luke Tweedy[1], Jennifer Geaves[3], Kirsty J. Martin[1], Kurt I. Anderson[1,4], Peter Brown[1], Sergio Lilla[1], Matthew P. Neilson[1], Petra Tafelmeyer[5], Sara Zanivan[1], Shehab Ismail[1,2], David M. Bryant[1,2], Nicholas C.O. Tomkinson[6], Luke H. Chamberlain[3], Grant S. Mastick[7], Robert H. Insall[‡1,2] and Laura M. Machesky[‡1,2]

Affiliations:
1. CRUK Beatson Institute, Switchback Road, Glasgow G61 1BD, UK
2. University of Glasgow Institute of Cancer Sciences, Switchback Road, Glasgow G61 1BD, UK
3. Strathclyde Institute of Pharmacy and Biomedical Sciences, University of Strathclyde, 161 Cathedral Street, Glasgow G4 0RE, UK
4. Present address: Francis Crick Institute, 1 Midland Road, King's Cross London, NW1 1AT
5. Hybrigenics Services, 3 Impasse Reille, 75014 Paris, France
6. WestCHEM, Department of Pure and Applied Chemistry, University of Strathclyde, Glasgow G1 1XL, UK
7. Department of Biology, University of Nevada, Reno, NV 89557, USA.

* First authors contributed equally
‡ Authors for correspondence contributed equally
l.machesky@beatson.gla.ac.uk
r.insall@beatson.gla.ac.uk

Abstract

Actin-based protrusions are reinforced through positive feedback, but it is unclear what restricts their size, or limits positive signals when they retract or split. We identify an evolutionarily conserved regulator of actin-based protrusion: CYRI (**CY**FIP-related **R**ac **i**nteractor) also known as Fam49. CYRI binds activated Rac1 via a Domain of Unknown Function DUF1394, shared with CYFIP, defining DUF1394 as a Rac1-binding module. CYRI-depleted cells have broad lamellipodia enriched in Scar/WAVE, but reduced protrusion-retraction dynamics. Pseudopods induced by optogenetic Rac1 activation in CYRI-depleted cells are larger and longer-lived. Conversely, CYRI overexpression suppresses recruitment of active Scar/WAVE to the cell edge, resulting in short-lived, unproductive protrusions. CYRI thus focusses protrusion signals and regulates pseudopod complexity by inhibiting Scar/WAVE-induced actin polymerization. It thus behaves like a "local inhibitor" predicted in widely accepted mathematical models, but not previously identified in cells. CYRI therefore regulates chemotaxis, cell migration and epithelial polarisation by controlling polarity and plasticity of protrusions.

Introduction

Cell migration is an ancient and fundamental mechanism whereby cells exert control over interactions with their environment. The actin cytoskeleton is the main driver of cell migration, with dozens of proteins controlling actin organisation[1]. Actin protrusions, or pseudopods, govern migration, however the feedback loops controlling assembly, splitting and disassembly of these structures is an area of active debate[2].

The Scar/WAVE complex is the main driver of Arp2/3-mediated branched actin networks underlying pseudopod generation. The complex consists of five subunits CYFIP, NCKAP1, Scar/WAVE, ABI, HSPC300 (nomenclature in Supplementary Table 1). The main Arp2/3 activating subunit, Scar/WAVE, is autoinhibited until signals trigger a conformational change, exposing an Arp2/3 activation sequence [3, 4]. The Scar/WAVE complex is recruited to acidic phospholipids in the plasma membrane via a patch of basic charges[3] and via interaction with the small GTPase Rac1[5-7].

Many motile cell types steer by splitting pseudopods into two or more daughters; selecting pseudopods from the split for retraction/maintenance provides a directional bias steering cells up chemotactic gradients[8]. Actin and associated signal transduction networks form excitable systems that propagate in waves and self-limit to drive protrusion and retraction[1, 9, 10]. Actin and associated cytoskeletal components likely control their own excitability in concert with signaling lipids, but dynamic interplay between "on" and "off" signals is essential for migration to be plastic and responsive.

Negative regulators of Arp2/3 complex include Gadkin, which sequesters Arp2/3 at the trans Golgi network and endosomes[11]. Another inhibitor, Arpin mimics the activating sequence of Scar/WAVE but inhibits the Arp2/3 complex [12]. Here, we describe a negative regulator of the Scar/WAVE complex, CYRI (encoded by the *FAM49* gene), an evolutionarily conserved protein that mimics the Rac1 interaction domain of CYFIP and promotes dynamic pseudopod splitting.

Results

CYRI is an evolutionarily conserved N-myristoylated protein with homology to CYFIP

We sought new Scar/WAVE complex interactors by precipitating GFP-fused NAP1 (for nomenclature see Supplementary **Table 1**) from *napA* knockout rescued *Dictyostelium* cells. Reversible formaldehyde crosslinking *in cellulo*[13] stabilised transient interactions and GFP-Trap immunocapture recovered Scar/WAVE, ABI, HSPC300 and PIR121. Another interactor was identified as Fam49 (FAMily of unknown function 49; **Fig 1a** and Supplementary **Table 2**). Although FAM49 did not co-precipitate with the Scar/WAVE complex in the absence of crosslinking, we focused on it for two reasons. Firstly, *FAM49* is highly conserved across evolution and is roughly co-conserved with the Scar/WAVE complex[14],[15] (**Supplementary Fig.1a**). Secondly, Pfam and InterPro identified FAM49 as uniquely sharing a DUF1394 domain with the Scar/WAVE complex subunit CYFIP (**Fig. 1b and Supplementary Fig.1b**). FAM49 proteins comprise mostly DUF1394, while CYFIP proteins contain a cytoplasmic fragile X interaction domain[16] **(Fig. 1b)**. We renamed FAM49 to CYRI for **<u>CY</u>**FIP-related **<u>R</u>**ac1 **<u>I</u>**nteractor, in mammals, represented by CYRI-A (FAM49-A) and CYRI-B (FAM49-B) and henceforth we use this nomenclature.

The DUF1394 region of CYFIP, highlighted in red (PDB 3P8C and **Fig. 1c)** partly overlaps with the published Scar/WAVE complex Rac1 interaction site, in particular R190 in CYFIP1[3] (**Fig. 1c**, Black arrow and blue balls). Modeling the structure of the DUF1394 of CYRI-B using Phyre2, reveals structural similarities with CYFIP **(**PDB 3P8C and **Fig. 1d)**. The analogous R161 of CYRI **(Fig 1d** blue sidechains, and **e** red box**)** is part of a highly conserved 33-amino acid stretch (>75% similarity) across diverse phyla (**Supplementary Fig. 1b-c**). R160 is also conserved in CYRI but replaced by lysine in CYFIP (**Fig. 1d-e and Supplementary Fig. 1b-c)**.

The N-terminal glycine-2 of CYRI proteins encodes a putative myristoylation site[17-19] **(Fig. 1f)**, which is not conserved in CYFIP. We confirmed the myristoylation of CYRI-B by assessing the incorporation of myristate analogue (C14:0-azide) onto G2 using CLICK chemistry *in cellulo*. Mutation of this glycine to alanine abolishes the CLICK signal **(Fig. 1 g-h)**.

In summary, we have defined CYRI, an evolutionarily conserved protein with a putative Rac1-binding DUF1394 module. Furthermore, N-terminal myristoylation suggests CYRI may dynamically associate with the plasma membrane[20], where active Rac1 stimulates the Scar/WAVE complex to catalyse lamellipodial expansion.

CYRI interacts directly with activated Rac1 *in vitro*

Homology between CYRI and CYFIP **(Supplementary Fig. 1b)**, suggested potential interaction with Rac1. Yeast two-hybrid screening with Rac1^{G12V} as bait retrieved CYRI-B from multiple cDNA libraries **(Supplementary Fig. 2a)**. The core interacting sequence of CYRI-B encompasses amino acids 30-236 (hereafter the Rac Binding Domain - RBD), **(Supplementary Fig. 2b-c**). GFP-RBD expressed in CHL-1 human melanoma cells interacted selectively with GST-Rac1^{Q61L} but not GST-Rac1^{WT}. Mutation of CYRI-B R160 or R161 (in GFP-RBD) to aspartic acid abrogated this interaction **(Fig. 2a-c and Supplementary Fig. 7).** GST-CYRI-B RBD and MBP-Rac1 also showed robust interaction **(Supplementary Fig. 2d-f and Supplementary Fig. 7)**. In this assay, CYRI does not co-precipitate with Rac1^{T17N}, Rac1^{G12V}, or Rac1 ^{WT}, likely due to the low affinity of CYRI-B for Rac1. However, the double mutant Rac1 $^{P29S/Q61L}$, recently shown to have a high affinity for the Scar/WAVE complex[21], displayed enhanced binding to CYRI-B RBD (~3-3.5-fold increase) over Rac1^{Q61L} but no enhanced binding to Pak1-CRIB (**Supplementary Fig. 2 d-f and Supplementary Fig. 7**). Using surface plasmon resonance, immobilised CYRI-B RBD specifically interacted with Rac1 ^{Q61L} with a K_d of 27 μM and the reverse assay, with Rac1 ^{Q61L} immobilised returned a K_d of 22 μM **(Fig. 2g)**. As CYRI-RBD shows no homology to CRIB (Cdc42 and Rac interaction binding) motifs, we probed the specificity of the interaction of CYRI between Rac1, RhoA and Cdc42. Once again, CYRI-RBD interacted robustly with

Rac1^{Q61L} but not with constitutively active RhoA^{Q63L} or Cdc42^{Q61L} **(Fig. 2d, Supplementary Fig. 2g-h and Supplementary Fig. 7)**. Thus CYRI-B RBD interacts specifically with active Rac1. Two conserved basic residues in the DUF1394 (conserved in CYFIP) mediate this interaction. This suggests a signal-regulated interaction between active Rac1 and CYRI, similar to the Rac1-CYFIP interaction, defining DUF1394 as an active Rac1 interaction module.

CYRI interacts with active Rac1 in cells

We next explored the Rac1-CYRI interaction in cells. Proximity ligation[22] revealed an interaction between Rac1^{WT} and CYRI-B in COS-7 cells, as well as a stronger interaction between Rac1^{Q61L} **(Fig. 2h-i and Supplementary Figure 2i-l)**. Mutation of key arginines in CYRI-B$^{R160/161}$-HA abolished this interaction and dominant negative Rac1^{T17N} showed no interaction **(Fig. 2 h-I and Supplementary Fig. 2i-l)**. Targetting either CYRI or Rac1A to mitochondria[23] **(Figure 2j)** in *Dictyostelium*, revealed that CYRI^{WT}, but not CYRI mutated for the analogous R155/156D, strongly co-recruits active Rac1A $^{P29S/Q61L}$. The Pearson's coefficient of fluorescence correlation (PCC) for Rac1A-mCherry-mito and the GFP-fusions revealed a PCC of the positive control CRIB-PBD 0.80 (SD: 0.20 – n=6); CYRI^{WT} 0.77 (SD: 0.21 – n=8 cells); and CYRI$^{R155/156D}$ 0.05 (SD: 0.12 – n=14 cells), where 1 = perfect, 0= no correlation and -1 = excluded. The PCC for Rac1A-mCherry and GFP-mito-fusions were: CRIB-PBD 0.33 (SD: 0.12 – n=6); CYRI ^{WT} 0.44 (SD: 0.19 – n=12 cells) and CYRI $^{R155/156D}$ -0.23 (SD: 0.05 – n=6 cells). CYRI-GFP did not co-localise with a control mitochondrial reporter mCherry-gemA$_{tail}$ (PCC = -0.06) (SD: 0.15 – n=6 cells). Thus, CYRI interacts with activated Rac1, mediated by key conserved arginines, in both mammalian and *Dictyostelium* cells.

CYRI opposes recruitment of the Scar/WAVE complex to lamellipodia

Knockdown or knockout of *CYRI-B* by siRNA or CRISPR in COS-7 or CHL-1 cells did not affect proliferation, but promoted unusually large and broad lamellipodia highly enriched in WAVE2 **(Fig. 3a-b, Supplementary Fig. 3a-g and Supplementary Fig. 7)**. Cells spread over a larger area and adopted a "fried-egg" phenotype, correlating with an increase in circularity **(Fig. 3c-d, Supplementary Fig. 3e-g)**. Expression levels of Scar/WAVE complex subunits are not obviously altered in *cyri-b* knockout cells **(Supplementary Fig. 3h and Supplementary Fig. 7)**. Cell area and circularity were both rescued by re-expression of untagged CYRI-B^{WT}, but not the Rac1-nonbinding R160/161D mutant **(Fig. 3e-f, Supplementary Figure 3i-k and Supplementary Fig. 7)**. CYRI-B^{G2A} which cannot be N-myristoylated failed to rescue the phenotype **(Fig. 3g-h, Supplementary 3l-m and Supplementary Fig. 7),** reinforcing the importance of CYRI lipid modification. *cyri* knockout *Dictyostelium* cells also showed enhanced recruitment of the Scar/WAVE complex (GFP-HSPC300 reporter) to a much broader leading edge **(Supplementary Fig. 3n – yellow dotted line and Supplementary Movie 1)**. Moreover, Scar/WAVE patches in *cyri* knockout cells are ill-defined but longer-lived, suggesting CYRI's ability to suppress Scar/WAVE complex activity outside of active protrusions. (**Supplementary Fig. 3n,** heat map**)**. We conclude that CYRI, via its interaction with active Rac1 and membrane targeting, opposes active Scar/WAVE complex at the plasma membrane and thus drives the formation of more focused and sharper lamellipodial protrusions.

To determine the requirement for Rac1 for the phenotype of *cyri-b* knockout cells, we co-depleted Rac1 and CYRI-B from mouse tail skin fibroblasts with ROSA26-Cre::ER^{T2+};*p16Ink4a*$^{-/-}$, *Rac1*$^{fl/fl}$ genotype[24], treated with hydroxytamoxifen (OHT, to induce deletion of *Rac1*) and then with siRNA against *Cyri-b* (**Supplementary Fig. 3o and Supplementary Fig. 7**). Deletion of *Rac1* led to a spindle-shaped morphology and a loss of lamellipodia as previously described [25-27]. Loss of CYRI-B did not cause excessive lamellipodia or rescue circularity in Rac-deleted cells **(Fig. 3i-k).** Thus, Rac1 is absolutely required for CYRI-B driven actin reorganisation.

The increased circularity of *cyri-b* depleted cells is reminiscent of Rac1 hyperactivation phenotypes[28], suggesting that CYRI-B might buffer Rac1 activity. Indeed, a dark acceptor mTq2-sREACH Raichu FRET probe[29, 30] showed a consistent increase in Rac1 signaling activity in CYRI-B depleted cells, as measured by FRET efficiency in both COS-7 **(Fig. 3l-m)** and CHL-1 cells **(Supplementary Figure 3p-q),** which was confirmed by biochemical pulldown **(Fig. 3n-o and Supplementary Fig. 7)**. Together, these data indicate an increase in Rac1 signaling activity in CYRI-B depleted cells. Conversely, inducible overexpression of untagged CYRI-B **(Supplementary Fig. 4a-b and Supplementary Fig. 7)** resulted in fractal-like lamellipodia, decreasing WAVE2 recruitment, cell area and circularity **(Fig. 4a-d, Supplementary Fig. 4c-f –** Vehicle-treated controls**)**. In parallel, overexpression of CYRI-B also drove a decrease in the Rac1 activity signal of the Raichu FRET probe (**Fig. 4e-f)** which was fully reversed by an R160/R161 double mutation **(Fig. 4g)**. Thus, CYRI-B opposes Rac1-Scar/WAVE mediated expansion of lamellipodia protrusions. Adding a GFP-tag to either end of CYRI-B interfered with its function, precluding dynamic analysis, likewise, available antibodies to Fam49B did not give specific staining by immunofluorescence, but CYRI-B-FLAG showed significant co-enrichment with WAVE2 at leading pseudopods **(Fig. 4h-i)**. Thus CYRI co-accumulates with WAVE2 at lamellipodia protrusions. Overall, *cyri-b* knockout cells show broader Scar/WAVE driven lamellipodia and increased Rac1 activation, supporting a role for CYRI-B as a buffer of Rac1 and Scar/WAVE complex activation activity at the leading edges of cells.

CYRI regulates the duration and extent of protrusions

We next sought to determine the consequences of CYRI-B depletion for lamellipodial actin dynamics. First, we observed actin dynamics live using fast frame-rate videos in CHL-1 cells expressing GFP-Lifeact **(Fig. 5a –** Left panel and **Supplementary Movie 2).** We tracked the cell edge and used unwrapped (polar) kymographs (**Fig. 5a** middle panels) to visualise and measure the area of protrusion **(**yellow colour**)** versus retraction **(**purple colour**)** over time. Control cells showed small but rapid bursts of actin-based protrusion (yellow patches on kymograph), while *cyri-b* knockouts had longer-lived less dynamic responses **(Fig. 5a,b)**. If CYRI-B buffers Rac1 at the lamellipodium, we speculated that *cyri-b* knockout cells would struggle to restrain protrusion formation upon Rac1 activation. To investigate this, we used the Rac1-LOV optogenetic probe, which triggers activation of Rac1 with blue light [31]. Rac1 was activated with pulses of blue light in a discrete area on the cell periphery **(Fig. 5c-d and Supplementary Movie 3)**. C*yri-b* knockout cells showed a more sustained and extensive protrusion response and increased peripheral propagation of lamellipodia **(Fig. 5e-g)**. Thus, CYRI-B limits Rac1- mediated activation of the Scar/WAVE complex and shortens the Rac1-activated protrusion.

CYRI focuses actin assembly in leading pseudopods to promote plasticity of migration

Plasticity of protrusion is important for directional migration, such as during chemotaxis. CHL-1 melanoma cells are normally nearly static when seeded at low density in 2D-culture, but *cyri-b* knockout cells migrated 1.5-2-fold faster (**Fig. 6a-b and Supplementary Movie 4**). C*yri-b* knockout cells frequently assumed a C-shape, with a broad spread lamellipodium at the front half of the cell and a convex rear which resembled the fast-moving goldfish keratocyte [32] **(Supplementary Fig. 5a** yellow arrows**, Supplementary Movie 4)**. C-shaped cells moved faster than the other common shapes **(Fig. 6c,d)** and C-shape correlated with faster migration **(Fig. 6e-f and Supplementary Fig. 5b-c)**. Lamellipodia need to be polarized and dynamic for efficient cell migration[27, 33], so when *cyri-b* knockout cells became polarized into a C-shape, they gained motility.

Since cells need to maintain plasticity of their lamellipodia to respond effectively to directional cues[34], we predicted that depletion of CYRI-B would affect chemotactic migration. CHL-1 cells are not chemotactic to serum, but WM852 melanoma cells are highly chemotactic[35]. Loss of CYRI-B (**Supplementary Fig. 5d-e and Supplementary Fig. 7**) severely affected chemotaxis of these cells towards a 10% serum gradient with no effect on basal speed; Knockouts often migrated very long distances in the opposite direction to the chemoattractant gradient, having lost the plasticity to reorient toward the gradient **(Fig. 6g-i and Supplementary Movie 5)**. Thus, CYRI-B strongly impacts how cells polarize and remodel their lamellipodia and reorient during directed migration.

CYRI promotes pseudopod splitting and opposes persistent migration in *Dictyostelium*

We examined *Dictyostelium* cells (Ax3, *cyri* knockout and rescue - **Supplementary Fig. 5f and Supplementary Fig. 7**) migrating under agarose up self-generated gradients of the chemoattractant folate[36] **(Supplementary Fig. 5g**). Similar to CHL-1 cells, *cyri* knockout cells were rounder, with blunted pseudopods **(Fig. 6j-k, Supplementary Movies 6-7).** *Dictyostelium* cells primarily turn by splitting their leading pseudopod into differently-oriented daughters[8]; automated segmentation and tracking revealed that *cyri* knockouts generated fewer protrusions/min **(Fig. 6l)** and showed fewer splits (from ~5/min to ~2/min, **Fig. 6m)** and decreased speed **(Fig. 6n)**. Cells still oriented towards the folate gradient, but their less efficient turning was clearly reflected by a smaller angle of turn between steps (**Supplementary Fig. 5h**). Thus, CYRI promotes pseudopod splitting in *Dictyostelium* cells, which is dispensible for gradient sensing, but compromises the speed of migration and reorientation while steering.

We rescued *Dictyostelium cyri* knockouts with CYRI^{WT} or CYRI$^{R155/156D}$ as stable, single-copy transfectants[37] under an actin15 promoter (**Fig. 6 j-n, Supplementary Movies 6-7**). CYRI^{WT} expressing cells exhibited more numerous fractal pseudopods as well as decreased circularity and enhanced frequency of protrusion generation and pseudopod splitting (**Fig. 6j-m**) even over WT cells. Rescue with CYRI^{WT} also restored cells' ability to turn during chemotaxis (**Supplementary Fig. 5h**).

Another widely- used chemotaxis assay involves a chemoattractant-filled microneedle introduced just next to *Dictyostelium* cells, inducing new pseudopods directly toward the needle, and consequently reorienting the cells. When cyclic-AMP (cAMP)-sensitive *cyri* knockout or rescue cells were challenged with cAMP in a needle assay, *cyri* knockouts were initially unable to form new pseudopods **(Fig. 6o)**, while CYRI^{WT} cells rapidly protruded pseudopods and reoriented toward the needle **(Figure 6o-p and Supplementary Movie 8)**. C*yri* knockouts eventually elongated and streamed toward the needle, but they maintained resistance to new pseudopod formation and rapid reorientation. Thus, cells that lack CYRI can still sense an attractant gradient, but their broad and unfocussed protrusions split rarely, and their diminished ability to generate new pseudopods cripples their response to changing gradients.

Modeling CYRI's role in pseudopod plasticity

Since CYRI affects plasticity of pseudopod dynamics, we likened its activity to the mathematical model of Meinhardt [38], where local inhibitors are recruited by an activation signal and limit the amount of cell edge devoted to pseudopods. Actin assembly pathways are not linear cascades, but rather feedback loops where positive stimulation is self-reinforcing and causes further activation until overcome by negative feedback[1, 10]. In models of migration based around positive feedback, a locally-acting inhibitor is also needed to destabilise existing pseudopods, so the cell can change direction. Without this, cells polarize, but cannot turn to migrate toward an attractant. We used a modified version of a published simulation[39] based on the Meinhardt model[38] to visualise the concentrations of the activator and the local inhibitor at the cell edge **(Supplementary Fig. 5i and Supplementary Movie 9)**, to illustrate the how CYRI-B regulates Rac1 and Scar/WAVE signaling. A peak in the activator (which represents active Rac1 and Scar/WAVE) results in the formation of a new pseudopod. The peak also causes an increase in the concentration of the local inhibitor, which is smaller and thus diffuses faster[38]. Initially, the inhibitor limits the lateral spread of the pseudopod (**Supplementary Fig. 5i**, panel 1); later, levels of inhibitor rise in the middle of the pseudopod, destabilizing it and causing a split (**Supplementary Fig. 5i**, panel 2). The weaker of the pseudopods then retracts and the stronger is reinforced until the cycle of inhibition catches up with it and re-starts the splitting cycle (**Supplementary Fig. 5i**, panels 3-4). The local inhibitor thus increases both the morphological complexity of the cell and the competition between pseudopods. This is supported by the lack of pseudopod splitting in *Dictyostelium* and our optogenetic data showing that protrusions in *cyri* knockout cells are more long-lived and spread laterally to a greater extent. Thus, Meinhardt's model offers insight into the role of CYRI proteins as local inhibitors, which enhance leading edge dynamics and add plasticity to the positive feedback loops driving migration.

CYRI-B regulates epithelial polarity via a Rac1-dependent mechanism

Finally, we tested a role for CYRI-B the polarized epithelial cyst [40, 41] where asymmetric Rac1 activation is also crucial. As cells form a cyst, they establish a lumen via selective membrane trafficking and polarized recruitment/activation of cytoskeletal components[42]. Specific spatial regulation is dependent on matrix and adhesions, but Rac1 activation also regulates lumen formation[43] and is specified by differential recruitment of the GEF TIAM1 across the cyst, leading to an apico-basal activation gradient[40]. We hypothesized that CYRI-B might help maintain the Rac1 activation gradient, allowing Scar/WAVE complex recruitment and activation to be spatially controlled during cyst formation. Indeed, knockdown of *CYRI-B* using shRNA in MDCK cells **(Supplementary Fig. 6a-b and Supplementary Fig. 7)** led to a multilumen phenotype during cyst formation, similar to deregulation of active Rac1 (**Figure 7a-b**, [42]). WAVE2 is normally prominently localized to the basolateral surfaces of the cysts, but mostly absent from the luminal surface, as marked by podocalyxin (PODXL) **(Fig. 7c)**. However, when CYRI-B was depleted, WAVE2 staining was increased at the luminal periphery coincident with PODXL staining **(Fig. 7c)**. Mislocalisation of the actin cytoskeleton machinery to cyst luminal surfaces results in aberrant orientation of the mitotic cleavage plane during polarized cell division, which occurred in *cyri-b* knockdown cysts **(Supplementary Fig. 6c-e)**. To test whether the multilumen phenotype was due to inappropriate Rac1 activation, we used moderate concentrations of either EHT1864 **(Fig. 7d-e)** or NSC23766 **(Supplementary Fig. 6f)** to dampen Rac1 activity; these both provided a substantial rescue. Thus, loss of CYRI-B destabilised epithelial polarity during the formation of epithelial cell cysts by allowing inappropriate Rac1-mediated recruitment of the actin machinery to the nascent luminal surface. CYRI-B thus maintains spatial regulation of activation of the Scar/WAVE complex by dynamic buffering of Rac1.

Discussion

CYRI is highly conserved and DUF1394 represents a Rac1 interaction module

CYRI proteins are highly conserved in eukaryotes and function as a Rac1 interaction module that directly limits Rac1-mediated lamellipodia extension. The DUF1394 domain of CYRI comprises the Rac1 binding site and is shared with CYFIP proteins of the Scar/WAVE complex. This interaction requires two highly conserved arginine/lysine residues, previously described on CYFIP1[3]. CYRI, like CYFIP1, is specific for activated Rac1 over RhoA and Cdc42. Myristoylation of glycine 2 of CYRI may allow recycling of CYRI between active pseudopods and the cytoplasm or membrane vesicles [44]. The Rac1-interacting formin FMNL2 is also myristoylated[45], implying potential common mechanisms for recruitment to actin protrusions. CYRI has no homology to GTPase activating proteins (GAPs), so it likely doesn't alter nucleotide hydrolysis by Rac1. Why would a cell need CYRI if it has Rac-GAPs? We propose CYRI could be a specific buffer for

Scar/WAVE-driven lamellipodia plasticity, rather than a general protein to turn off Rac1.

CYRI opposes recruitment of active Scar/WAVE complex to leading edges and promotes plasticity

Modulating the levels of CYRI differently affected cell speed in the cell types we assayed. While this may seem paradoxical, the basal speeds of these cell types and modes by which they migrate are different. Furthermore, migration speed is multiparametric, being the result of a combination of protrusion, adhesion and directionality/persistence. Migration speed is thought to require optimal levels of Rac1 activation and can be slowed by too little/much active Rac1[33]. *Dictyostelium* are optimized by nature to be fast-moving and relatively non-adhesive, so nearly any change will result in slower migration. In contrast, the speed of adhesive slow-moving cancer cells may benefit from removing the brakes on Rac1 activity.

Negative regulators of Arp2/3 complex have been described [11, 12, 46], but thus far, CYRI is the only negative regulator of the Scar/WAVE complex. Importantly, it is widely conserved in evolution along with the Scar/WAVE complex, so is a universal negative regulator. CYRI and CYFIP likely resulted from an ancient gene duplication and retained the same Rac1 binding function, placing CYRI as a Meinhardt local inhibitor[38]. But a local inhibitor should be present at high enough concentration to compete with the activator. A recent quantitative mass spectrometry study estimated concentrations of CYRI-B to be 4-fold higher in protein copy number than Scar/WAVE complex [47] in 3 of 4 cell lines (A549 4-fold, HepG2 5-fold, PC3 4.4-fold and U87 0.53-fold, based on comparison with CYFIP1). Thus, there is likely enough CYRI-B in cells to compete with the Scar/WAVE complex for Rac1 binding.

CYRI provides spatiotemporal regulation of the connection between Rac1 and Scar/WAVE complex

Cell migration involves cycles of protrusion and retraction coupled with adhesion to produce forward locomotion [48]. Cells with wild-type levels of CYRI showed rapid protrusion-retraction dynamics indicative of transient activation of the Scar/WAVE complex (e.g. kymograph **Fig. 5a**). *cyri* knockouts showed broader and more sustained lamellipodia and increased Scar/WAVE recruitment, placing CYRI as a key part of the feedback loop controlling leading edge actin dynamics, in line with Arpin, a negative regulator of the Arp2/3 complex [12] and coronin, which positively regulates Rac1 activation [49, 50,1]. Breaking the feedback loop by deleting CYRI affected both Scar/WAVE recruitment and Rac1 signalling activity. Thus, the actin machinery feeds back to Rac1 dynamically. This dynamic feedback is necessary for cells to change direction and respond with plasticity to stimuli such as chemotactic gradients.

CYRI also regulates polarized function of Rac1-Scar/WAVE complex in epithelial cells in 3D. Epithelial cells establish a Rac1 gradient that maintains polarity by asymmetric distribution of β2-syntrophin and Par3 [40]. Par3, localized apically, inhibits the Rac-GEF TIAM1, while β2-syntrophin, localized basally, activates

TIAM1. This gradient is required for proper luminogenesis. CYRI helps direct formation of a single polarized lumen by regulating the Rac1 gradient required for proper spindle orientation. A role for CYRI in epithelia could have broad implications for development and cancer.

Cell migration is the outcome of feedback loops that control the dynamics of cell shapes [10, 38, 51-53]. Travelling and spreading wave patterns (for example [10, 51]) manifest in actin-based protrusions, implying positive feedback loops. However, negative feedback is also required[38] to prevent uniform activation. Actin and actin-binding proteins can comprise an excitable system [10, 52] also modulated by systems involving small GTPases, kinases and signaling lipids e.g.[9]. Our data imply that CYRI acts at the interface; by competing with Scar/WAVE (an actin-nucleating complex) for Rac1 (a small GTPase) it connects signaling with actin polymerization, moderating excitable behaviours.

In conclusion, we propose that CYRI is a highly conserved regulator of the dynamics of the Rac1 – Scar/WAVE pathway, providing plasticity and adding complexity to leading edge dynamics.

Acknowledgements

We thank Margaret O'Prey and the BAIR imaging facility for help with microscopy, Chloe Tesniere for careful work with CYRI overexpression plasmids, Michael Mcilwraith for help with protein purification, Benjamin Tyrell for isolation of the inducible *Rac* $^{fl/fl}$ fibroblasts, Klemens Rottners and Matthias Schaks for technical advice and discussion, Roland Wedlich-Söldner for the GFP-Lifeact construct. We thank CRUK for core funding to L.M.M. (grant A15673), R.H.I. (grant A19257) and S.Z. (C596/A12935), BBSRC for funding to L.H.C and N.C.O.T (BB/L022087/1), and NIH for funding to G.S.M (NIH RO1 EY025205). Fundação para a Ciência e a Tecnologia, Portugal (PhD scholarship ref. SFRH/BD/69003/2010 awarded to JMB).

Author contributions

R.H.I. and J.B. conceived and carried out the initial screen and recognized the similarity of CYRI to CYFIP. L.F. designed and carried out the majority of the experiments on mammalian CYRI-B. L.M.M., R.H.I. and L.F. conceived the study and wrote the paper. P.A.T. designed and constructed the mitochondrial relocalisation tools and carried out the *Dictyostelium* experiments in Figs 2 and 6. K.M. and K.I.A. designed the Raichu FRET probe and with L.F. carried out the FRET experiments. P.B. and L.F. carried out the surface plasmon resonance experiments. J.G., N.C.O.T., and L.C. synthesized probes for, advised on and carried out the myristoylation experiments with L.F. S.L. and S.Z. carried out and analysed the mass spectrometry with L.F. and J.B. P.A.T., G.S.M., J.A.W., H.J.S., L.T and S.I. provided essential advice, carried out experiments and analysis of data. M.N. and R.H.I. constructed the model and advised on its use.

Competing interests

Petra Tafelmeyer works with Hybrigenics, which performs yeast 2-hybrid screening for commercial purposes.

Figure Legends

Figure 1 - CYRI (Fam49) proteins show homology to CYFIP and contain a putative Rac1 interaction motif

a – Volcano plot illustrating pooled results from four LC-MS/MS experiments showing comparison of formaldehyde crosslinked proteins co-immunoprecipitating with GFP or GFP-NAP1 in *Dictyostelium napA* knockout cells. Color-coding based on two-tailed Welch's t test difference. Curved line is 5% false discovery rate. Identified interactors are labeled with gene symbols and presented in **Supplementary Table 2**. (n=4 independent experiments).

b – Schematic of human CYFIP1/2 and CYRI-A/B showing amino acid numbers and domains. Common DUF1394 domain (Pfam PF07159) in red and CYFIP1/2 C-terminal cytoplasmic Fragile X Mental Retardation FMR1-interacting domain (FragX-IP, Pfam PF05994) in light green.

c - Two views of ribbon crystal structure of the Scar/WAVE complex (PDB 3P8C)[2]. NCKAP1 in lilac, CYFIP1 in light green and red, Scar/WAVE in peach, HSPC300 in yellow and ABI1 in orange. DUF1394 is red, with putative Rac1 interaction residues in blue and highlighted by arrows.

d – Phyre prediction of structure of the DUF1394 domain of CYRI-B. The putative Rac1-binding domain of CYRI is blue with Arg160 and Arg161 indicated as a stick representation.

e - Sequence alignment of the putative Rac1-binding domain of CYRI in different organisms. The CYFIP Lys189 and Arg190 equivalent residues are well conserved in CYRI (Arg160 and Arg161) and are highlighted in red.

f - Sequence alignment covering the N-terminal region of CYRI from representative evolutionarily diverse eukaryotes. UniProt accession numbers are reported. Color code represents the number of entries with an identical amino acid at this position. The glycine in the 2nd position (highlighted red) is a putative myristoylation site.

g-h - CLICK chemistry analysis of the glycine 2 of CYRI-B. Myristoylation was labeled in HEK293T cells and measured by incorporation of myristate-azide (green) in GFP, CYRI-B^{WT}-GFP or CYRI-B^{G2A}-GFP mutant transfected cells (magenta), following GFP immunoprecipitation. Molecular markers shown left (**g**) See also **Supplementary Fig. 7 and Supplementary Table 6**. Relative incorporation was quantified by densitometry and reported in (**h**). One way ANOVA with Tukey post-test was applied. *** $p<0.001$. (n=3 independent assays). Bar graph represents mean and S.E.M.

Figure 2 - CYRI proteins interact with active Rac1

a-c - Western blot from pulldown of GST control, GST-Rac1^{WT} or GST-Rac1^{Q61L} beads, with cell lysate expressing either GFP alone, positive control PAK1 eCFP-CRIB-PBD, GFP-RBD^{WT}, GFP-RBD^{R160D} or GFP-RBD^{R161D} (**a**). Densitometry (**b-c**). (n=3 independent experiments for GFP-RBD^{R160D} and GFP-RBD^{R161D} and n=4 for GFP and GFP-RBD^{WT}).

d-f - Western blot pulldown of GST control, GST-Rac1^{P29S} or GST-Rac1^{Q61L} or GST-Rac1$^{P29S/Q61L}$ beads, with cell lysate expressing controls or CYRI GFP-RBD^{WT} (**d**). Densitometry (**e-f**). (n=3 independent experiments).

g – Steady state SPR binding curves between Rac1^{Q61L} and CYRI-B-RBD. Left: GST-CYRI-B immobilized vs increasing concentrations of Rac1^{Q61L}. Right: His-Rac1 immobilised vs increasing CYRI-B RBD. Simple 1:1 binding model. K_d = equilibrium dissociation constant, A.U. = arbitrary units.

h-i Proximity ligation assay COS-7 cells on laminin co-expressing CYRI and Rac1 constructs. PLA signal (yellow), F-actin (magenta) and nuclei (blue). See **Supplementary Fig. 2** -negative controls. Data pooled across 4 independent experiments in **(i)**. One-way ANOVA with Dunn's post-test between CYRI-B^{WT} and MYC-Rac1 constructs. Two-tailed Mann Whitney test between CYRI-B^{WT} and CYRI-B$^{R160/161D}$ for each MYC-Rac1 construct. n.s. $p > 0.05$, ** $p \leq 0.01$, *** $p \leq 0.001$. (anti-HA n=55; anti-Myc n=54; Myc-WT/WT-HA n=55; Myc-WT/R160-161D-HA n=55; Myc-T17N/WT-HA n=63; Myc-T17N/ R160-161D-HA n=84; Myc-Q61L/WT-HA n=69; Myc-Q61L/ R160-161D-HA n=65, where n=cells)
Scale bar, 50 µm.

j - Mitochondrial recruitment of CYRI-GFP to Rac1A-mCherry-mito (Forward) or Rac1A$^{P29S/Q61L}$mCherry to CYRI-GFP-mito (Reverse) in Ax3 *D. discoideum*. (>300 mitochondria/cell). Far right panels negative control lacking Rac1. Scale bar, 5 µm

a-j represent at least three biologically independent experiments. Graphs show mean and S.E.M. Source data in **Supplementary Table 6**. Unprocessed Western blots in **Supplementary Figure 7**.

Figure 3 - Loss of CYRI-B increases Rac1-mediated Scar/WAVE localisation to lamellipodia

a-d - Immunofluorescence of control (Ctr) or *cyri-b* knockdown (siRNA #1 and 2) COS-7 showing WAVE2 (green), nuclei (blue) and F-actin (magenta). Scale bar = 50 µm. Box insets zoom, scale bar = 10 µm.
Ratio of WAVE2 (yellow dotted line) *vs* total cell perimeter (**b**). Cell area in (**c**) and circularity (**d**). One-way ANOVA with Dunn's post-test n.s. $p > 0.05$, *** $p \leq 0.001$. (**a-c:** Scramble n=111; #1 n=95; #2 n=96 – **d**: Scramble n=115; #1 n=92; #2 n=98) n represents cells in a-o.

e-f –COS-7 with *cyri-b* knockdown and rescued with pLIX-mVenus si-resistant CYRI-B (WT or R160/161D) or empty vector (EV). (see **Supplementary Fig. 3l**). Cell area (**e**) and circularity (**f**). One-way ANOVA with Dunn's post-test n.s. $p > 0.05$, *** $p \leq 0.001$. (Scramble/EV n=78; Scramble/WT n=58; Scramble/R160-161D n=66; #1/EV n=66; #1/WT n=64; #1/R160-161D n=60).

g-h – Control or *cyri-b* knockdown COS-7 with pLIX-mVenus and si-resistant CYRI-B (WT or G2A mutant) or EV. Cell area (**g**) and circularity (**h**). One-way ANOVA with Dunn's post-test n.s. $p > 0.05$, *** $p \leq 0.001$. (Scramble/EV n=70; Scramble/WT n=52; Scramble/G2A n=46; #1/EV n=63; #1/WT n=64; #1/G2A n=65)

i-k - Control (DMSO) or *rac1* knockout (OHT) mouse tail fibroblasts with Scramble (siCtr) or *Cyri-B* siRNA, showing WAVE2 (**i**). Scale bar = 50 µm. Lamellipodial WAVE2 (**j**) and circularity (**k**). One-way ANOVA with Dunn's post-test *** $p \leq 0.001$. two-tailed Mann Whitney test between OHT and control. ### $p \leq 0.001$. (n=30 cells/condition).

l-m - FLIM/FRET of mTq2-sREACH in control (siCtr) or *cyri-b* knockdown (siCYRI-B #1 and #2) COS-7. Jet2 color code (left) average lifetime, 1-4 ns blue to red. (**l**). FRET efficiency (**m**). One-way ANOVA with Dunn's post-test. *** $p \leq 0.001$. (Scramble n=61; #1 n=61, #2 n=63)
Scale bar = 50 µm

n-o - Active Rac1 pulldown comparing control CrispR (Vector^{Ctr}) or independent *cyri-b* CrispR (#1 and #2) COS-7 lines. See also Supplementary Fig. 7.

Data in a-o represent three biologically independent experiments. All cells plated on laminin. See also Supplementary Table 6.
Bar and scatter plots show data points with mean and S.E.M.
Whisker plots show 10-90 percentile, median (bar) and mean (cross).

Figure 4 - Overexpression of CYRI-B opposes Rac1-mediated Scar/WAVE recruitment to the leading edge

a-d - Immunofluorescence of doxycycline-induced control empty vector (EV) or CYRI-B overexpression in COS-7 cells and fixed after 4h showing WAVE2 (magenta), nuclei (blue) and GFP (green). Scale bar = 50 µm. Insets show zoom of white dashed field. Scale bar = 10 µm (**a**). WAVE2 ratio and circularity in (**b**) and (**c**) respectively. Cell area quantification was based on phalloidin staining (**d**). Two-tailed Mann-Whitney test *** $p \leq 0.001$. (Dox/EV n=73; Dox/CYRI-B n=93) n represents cells in a-i

e-f - FLIM/FRET experiment with mTq2-sREACH Raichu Rac1 showing vehicle or doxycycline-treated COS-7 cells expressing a control empty vector (EV) or CYRI-B. The jet2 color code (bar at top) shows the average lifetime of the probe, spanning 1-4 ns (blue to red) (**e**). Quantification of the FRET efficiency (**f**). Two-tailed Mann-Whitney test n.s. $p > 0.05$, *** $p \leq 0.001$. (Veh/EV n=47; Veh/CYRI-B n=46; Dox/EV n=62; Dox/CYRI-B n=62)
Scale bar = 50 µm.

g - FRET efficiency obtained from control (EV) or COS-7 cells overexpressing CYRI^{WT} or CYRI-B$^{R160/161D}$ after doxycycline induction. One-way ANOVA with Dunn's post-test was performed. n.s. $p > 0.05$, *** $p \leq 0.001$. (EV n=59; WT n=62; R160/161D n=63).

h-i - Immunofluorescence of COS-7 cells transfected with CYRI-B-FLAG and stained for FLAG-tag (green), F-actin (top row) or WAVE2 (bottom row) (magenta) and nuclei (blue). Scale bar = 50 µm (**h**). FLAG-staining is quantified by normalizing the fluorescence intensity running across 17 representative cells and ending at the protrusive end (normalized distance: 1=protrusive end and 0=opposite end). FLAG-tag and F-actin staining intensity are shown in green and magenta respectively (**i**) (n=17).

Data in a-i represent three biologically independent experiments.
See also Supplementary Table 6.
Bar and scatter plots show data points with mean and S.E.M.
Whisker plots show 10-90 percentile, median (bar) and mean (cross).

Figure 5 - CYRI-B controls the duration and extent of Rac1-mediated protrusions

a - Control (Vector ^{Ctr}) and *cyri-b* CrispR knockout CHL-1 cells on laminin expressing GFP-LifeAct, recorded for 3 minutes at 1 frame/sec. The cell periphery (magenta) is tracked using the GFP-LifeAct signal (green) (Left panel). The membrane is unravelled from the orange arrow and a representative polar kymograph of the changes in membrane dynamics over time between control (Vector ^{Ctr} - Top) and *cyri-b* CrispR knockout (Bottom) CHL-1 cells is shown. Membrane extensions (positive values) are visualised in yellow through to orange, while retractions (negative values) are purple-blue (Middle panel). Thresholding of the kymograph to remove noise (values $\geq + 0.6$) reveals protrusions over time (white signal – Right panel)
Still from movie S2. Scale bar = 25 µm.

b - Box plot representing the distribution of the average protrusion lifetime for each individual cell. Whisker plots represent mean and S.D. Two-tailed Mann Whitney test. *** $p \leq 0.001$. (n= 20 cells/condition)

c - Schematic representation showing protruding (blue) and retracting (magenta) area following photoactivation of Rac1-LOV probe. Photo activation area (green circle) was used as the origin to measure the maximal protrusion distance (outward - black line) and the longest uninterrupted lateral spread of the protrusion (red dotted line)

d - Still pictures from videos of photoactivation time course showing selected cells from DMSO (Control) or OHT-treated (knockout) immortalized CRE-ER^{T2+} *Cyri-B*$^{fl/fl}$ MEFs on fibronectin. Endpoint overlay as from schematic (**c**). Scale bar = 25 µm.

e-f - Quantification of the protrusion distance (**e**) and the spread of activation (**f**) between control (DMSO) or *cyri-b* knockout (OHT) MEFs.
Error bars represent 95% CI. Unpaired two-tailed t-test (**e**) and two-tailed Mann-Whitney test (**f**). *** $p \leq 0.001$, **** $p \leq 0.0001$. (DMSO n=29 cells; OHT n=30 cells).

g - Kymograph representation before and after photo activation. Membrane extensions are visualised in yellow through to orange, while retractions are observed in purple-blue. Time of photoactivation is highlighted by a white dotted line.

Data in a-g represent three biologically independent experiments.
See also Supplementary Table 6.

Figure 6 - CYRI modulates protrusion plasticity during directional migration

a-c – Spider plots CrispR and control CHL-1 cells on collagen-I, 17h (**a**) (See **movie S4)**. Black and red lines = distance > or <100 µm respectively. Average speed (**b**). **(c**) Duration as C-shape **(b,c)** One-way ANOVA with Dunn's post-test **(b)** (Ctr n=161; #1 n=228; #2 n=178). **(c)** (Ctr n=45; #1 n=53; #2 n=42). n=cells in a-p.

d - Speed of CrispR and control CHL-1. One-way ANOVA with Dunn's post-test (Ctr n=45; #1 n=53; #2 n=42)

e-f - Immunofluorescence of CrispR and control CHL-1 on collagen. F-actin (magenta) and nuclei (blue) (**e**). Scale bar = 50 µm. (**f**). Two-tailed Chi-square test (95% confidence). (Ctr n=276; #1 n=216; #2 n=210)

g-i - Spider and Rose plots of CrispR and control WM852 cell chemotaxis (**g**) (see **movie S5**). Red-dashed lines 95% confidence interval for mean direction. Cosθ (chemotactic index) (**h**) average speed (**i**). Two-tailed unpaired t-test. (Ctr n=129; #1 n=132; #2 n=151).

j-n - DIC pictures from *Dictyostelium* under-agarose chemotaxis (**j**) (see **movie S6**). Scale bar = 10 µm. Circularity (**k**), protrusions (**l**), split frequency (**m**), and speed (**n**). One-way ANOVA with Dunn's post-test. (**k**: WT n=360; *cyri* KO n=352; *cyri* KO + CYRI ^{WT} n=480; *cyri* KO + CYRI $^{R155/156}$ n=240 - **l**: WT n=45; *cyri* KO n=57; *cyri* KO + CYRI ^{WT} n=53; *cyri* KO + CYRI $^{R155/156}$ n=31 - **m**: WT n=42; *cyri* KO n=62; *cyri* KO + CYRI ^{WT} n=46; *cyri* KO + CYRI $^{R155/156}$ n=33 - **n**: WT n=2389; *cyri* KO n=2460; *cyri* KO + CYRI ^{WT} n=3024; *cyri* KO + CYRI $^{R155/156}$ n=1169)

o-p - Needle assay using WT or *cyri* knockout Ax3 cells with cAMP (see also **movie S8**) (yellow start). Scale bar = 25 µm (**o**). Spider plots during 0-100s (**p**). (WT n=86; *cyri* KO n=79)

a-p represent three biologically independent experiments with mean and S.E.M unless indicated. Whisker plots 10-90 percentile (**b, k-m**) and 1-99 percentile (**n**) with median (bar) and mean (cross). n.s. $p>0.05$, * $p\leq0.05$, ** $p\leq0.01$, *** $p\leq0.001$.
See Supplementary Table 6.

Figure 7 - CYRI-B regulates Rac1-dependent recruitment of Scar/WAVE complex during epithelial cystogenesis

a-b – Immunofluorescence of control (Vector ^{Ctr}) or *cyri-b* shRNA knockdown (#1 and #2) MDCK cysts fixed after 5 days of culture and stained for Podocalyxin (PODXL) (green), F-actin (red) and nuclei (blue). Top row is a confocal section and bottom row represents Z-maximal projection intensity of PODXL staining. Scale bar = 50 μm (**a**). Quantification of lumens in (**b**). One-way ANOVA with Dunn's post-test. *** $p<0.001$. (Ctr n=1000 cysts, #1 n=1000 cysts, #2 n=800 cysts).

c - Immunofluorescence of control (Vector ^{Ctr}) or *cyri-b* shRNA knockdown (#1 and #2) MDCK cysts stained for WAVE2 (green) and Podocalyxin (PODXL) (red) after 5 days of culture. Inverted LUT images, merge and representative surface profile plots shown. PODXL (red) and WAVE2 (green) staining intensity was measured along the blue line. Scale bar = 9 μm. Insets provide a magnified view of the dotted square area. Scale bar = 5 μm.

d-e – Immunofluorescence of control (Vector ^{Ctr}) or *cyri-b* shRNA knockdown (#1 and #2) MDCK cysts grown during 5 days, treated or not with 50 nM EHT1864 and stained for Podocalyxin (PODXL). Pictures represent the Z-maximal projection intensity from a representative z-stack running across the entire cyst volume. Scale bar = 50 μm (**d**). Number of lumens per cyst was quantified for vehicle or EHT1864-treated cysts and plotted in (**e**). One-way ANOVA with Dunn's post-test between control (Vector ^{Ctr}), shCYRI-B #1 and shCYRI-B #2 whereas unpaired two-tailed t-test between vehicle and drug-treated cyst. n.s. $p>0.05$, ** $p\leq0.01$ *** $p\leq0.001$. (250 cysts/condition)

Data in a-e represent N=3 biologically independent experiments.
Bar and scatter plots show data points with mean and S.E.M.
Whisker plots show 10-90 percentile, median (bar) and mean (cross).
See also Supplementary Table 6.

References

1. Krause, M. & Gautreau, A. Steering cell migration: lamellipodium dynamics and the regulation of directional persistence. *Nat Rev Mol Cell Biol* **15**, 577-590 (2014).
2. Insall, R. The interaction between pseudopods and extracellular signalling during chemotaxis and directed migration. *Curr Opin Cell Biol* **25**, 526-531 (2013).
3. Chen, Z. *et al.* Structure and control of the actin regulatory WAVE complex. *Nature* **468**, 533-538 (2010).
4. Davidson, A.J. & Insall, R.H. Actin-based motility: WAVE regulatory complex structure reopens old SCARs. *Curr Biol* **21**, R66-68 (2011).
5. Hoeller, O. *et al.* Gbeta Regulates Coupling between Actin Oscillators for Cell Polarity and Directional Migration. *PLoS Biol* **14**, e1002381 (2016).

6. Veltman, D.M., King, J.S., Machesky, L.M. & Insall, R.H. SCAR knockouts in Dictyostelium: WASP assumes SCAR's position and upstream regulators in pseudopods. *J Cell Biol* **198**, 501-508 (2012).
7. Weiner, O.D. *et al.* Hem-1 complexes are essential for Rac activation, actin polymerization, and myosin regulation during neutrophil chemotaxis. *PLoS Biol* **4**, e38 (2006).
8. Andrew, N. & Insall, R.H. Chemotaxis in shallow gradients is mediated independently of PtdIns 3-kinase by biased choices between random protrusions. *Nat Cell Biol* **9**, 193-200 (2007).
9. Devreotes, P.N. *et al.* Excitable Signal Transduction Networks in Directed Cell Migration. *Annu Rev Cell Dev Biol* **33**, 103-125 (2017).
10. Graziano, B.R. & Weiner, O.D. Self-organization of protrusions and polarity during eukaryotic chemotaxis. *Curr Opin Cell Biol* **30**, 60-67 (2014).
11. Maritzen, T. *et al.* Gadkin negatively regulates cell spreading and motility via sequestration of the actin-nucleating ARP2/3 complex. *Proc Natl Acad Sci U S A* **109**, 10382-10387 (2012).
12. Dang, I. *et al.* Inhibitory signalling to the Arp2/3 complex steers cell migration. *Nature* **503**, 281-284 (2013).
13. Sobczyk, G.J., Wang, J. & Weijer, C.J. SILAC-based proteomic quantification of chemoattractant-induced cytoskeleton dynamics on a second to minute timescale. *Nat Commun* **5**, 3319 (2014).
14. Keeling, P.J. *et al.* The tree of eukaryotes. *Trends Ecol Evol* **20**, 670-676 (2005).
15. Veltman, D.M. & Insall, R.H. WASP family proteins: their evolution and its physiological implications. *Mol Biol Cell* **21**, 2880-2893 (2010).
16. Bramham, C.R., Jensen, K.B. & Proud, C.G. Tuning Specific Translation in Cancer Metastasis and Synaptic Memory: Control at the MNK-eIF4E Axis. *Trends Biochem Sci* **41**, 847-858 (2016).
17. Bienvenut, W.V. *et al.* Comparative large scale characterization of plant versus mammal proteins reveals similar and idiosyncratic N-alpha-acetylation features. *Mol Cell Proteomics* **11**, M111 015131 (2012).
18. Broncel, M. *et al.* Multifunctional reagents for quantitative proteome-wide analysis of protein modification in human cells and dynamic profiling of protein lipidation during vertebrate development. *Angew Chem Int Ed Engl* **54**, 5948-5951 (2015).
19. Yang, W., Di Vizio, D., Kirchner, M., Steen, H. & Freeman, M.R. Proteome scale characterization of human S-acylated proteins in lipid raft-enriched and non-raft membranes. *Mol Cell Proteomics* **9**, 54-70 (2010).
20. Lanyon-Hogg, T., Faronato, M., Serwa, R.A. & Tate, E.W. Dynamic Protein Acylation: New Substrates, Mechanisms, and Drug Targets. *Trends Biochem Sci* (2017).
21. Chen, B. *et al.* Rac1 GTPase activates the WAVE regulatory complex through two distinct binding sites. *Elife* **6** (2017).
22. Soderberg, O. *et al.* Characterizing proteins and their interactions in cells and tissues using the in situ proximity ligation assay. *Methods* **45**, 227-232 (2008).
23. Robinson, M.S., Sahlender, D.A. & Foster, S.D. Rapid inactivation of proteins by rapamycin-induced rerouting to mitochondria. *Dev Cell* **18**, 324-331 (2010).

24. Walmsley, M.J. *et al.* Critical roles for Rac1 and Rac2 GTPases in B cell development and signaling. *Science* **302**, 459-462 (2003).

25. Li, A. *et al.* Activated mutant NRas(Q61K) drives aberrant melanocyte signaling, survival, and invasiveness via a Rac1-dependent mechanism. *J Invest Dermatol* **132**, 2610-2621 (2012).

26. Li, A. *et al.* Rac1 drives melanoblast organization during mouse development by orchestrating pseudopod- driven motility and cell-cycle progression. *Dev Cell* **21**, 722-734 (2011).

27. Steffen, A. *et al.* Rac function is crucial for cell migration but is not required for spreading and focal adhesion formation. *J Cell Sci* **126**, 4572-4588 (2013).

28. Ridley, A.J., Paterson, H.F., Johnston, C.L., Diekmann, D. & Hall, A. The small GTP-binding protein rac regulates growth factor-induced membrane ruffling. *Cell* **70**, 401-410 (1992).

29. Martin, K.J. *et al.* Accepting from the best donor; analysis of long-lifetime donor fluorescent protein pairings to optimise dynamic FLIM-based FRET experiments. *PLoS One* **13**, e0183585 (2018).

30. Nakamura, T., Kurokawa, K., Kiyokawa, E. & Matsuda, M. Analysis of the spatiotemporal activation of rho GTPases using Raichu probes. *Methods Enzymol* **406**, 315-332 (2006).

31. Wu, Y.I. *et al.* A genetically encoded photoactivatable Rac controls the motility of living cells. *Nature* **461**, 104-108 (2009).

32. Keren, K., Yam, P.T., Kinkhabwala, A., Mogilner, A. & Theriot, J.A. Intracellular fluid flow in rapidly moving cells. *Nat Cell Biol* **11**, 1219-1224 (2009).

33. Pankov, R. *et al.* A Rac switch regulates random versus directionally persistent cell migration. *J Cell Biol* **170**, 793-802 (2005).

34. Insall, R. & Andrew, N. Chemotaxis in Dictyostelium: how to walk straight using parallel pathways. *Curr Opin Microbiol* **10**, 578-581 (2007).

35. Muinonen-Martin, A.J. *et al.* Melanoma cells break down LPA to establish local gradients that drive chemotactic dispersal. *PLoS Biol* **12**, e1001966 (2014).

36. Tweedy, L., Knecht, D.A., Mackay, G.M. & Insall, R.H. Self-Generated Chemoattractant Gradients: Attractant Depletion Extends the Range and Robustness of Chemotaxis. *PLoS Biol* **14**, e1002404 (2016).

37. Kuspa, A. & Loomis, W.F. Tagging developmental genes in Dictyostelium by restriction enzyme-mediated integration of plasmid DNA. *Proc Natl Acad Sci U S A* **89**, 8803-8807 (1992).

38. Meinhardt, H. Orientation of chemotactic cells and growth cones: models and mechanisms. *J Cell Sci* **112 (Pt 17)**, 2867-2874 (1999).

39. Neilson, M.P., Mackenzie, J.A., Webb, S.D. & Insall, R.H. Use of the parameterised finite element method to robustly and efficiently evolve the edge of a moving cell. *Integr Biol (Camb)* **2**, 687-695 (2010).

40. Mack, N.A. *et al.* beta2-syntrophin and Par-3 promote an apicobasal Rac activity gradient at cell-cell junctions by differentially regulating Tiam1 activity. *Nat Cell Biol* **14**, 1169-1180 (2012).

41. Mangan, A.J. *et al.* Cingulin and actin mediate midbody-dependent apical lumen formation during polarization of epithelial cells. *Nat Commun* **7**, 12426 (2016).

42. Overeem, A.W., Bryant, D.M. & van, I.S.C. Mechanisms of apical-basal axis orientation and epithelial lumen positioning. *Trends Cell Biol* **25**, 476-485 (2015).

43. Yagi, S., Matsuda, M. & Kiyokawa, E. Suppression of Rac1 activity at the apical membrane of MDCK cells is essential for cyst structure maintenance. *EMBO Rep* **13**, 237-243 (2012).

44. Jiang, H. *et al.* Protein Lipidation: Occurrence, Mechanisms, Biological Functions, and Enabling Technologies. *Chem Rev* **118**, 919-988 (2018).

45. Grobe, H., Wustenhagen, A., Baarlink, C., Grosse, R. & Grikscheit, K. A Rac1-FMNL2 signaling module affects cell-cell contact formation independent of Cdc42 and membrane protrusions. *PLoS One* **13**, e0194716 (2018).

46. Madasu, Y. *et al.* PICK1 is implicated in organelle motility in an Arp2/3 complex-independent manner. *Mol Biol Cell* **26**, 1308-1322 (2015).

47. Wisniewski, J.R., Hein, M.Y., Cox, J. & Mann, M. A "proteomic ruler" for protein copy number and concentration estimation without spike-in standards. *Mol Cell Proteomics* **13**, 3497-3506 (2014).

48. Meacci, G. *et al.* alpha-Actinin links extracellular matrix rigidity-sensing contractile units with periodic cell-edge retractions. *Mol Biol Cell* **27**, 3471-3479 (2016).

49. Swaminathan, K., Muller-Taubenberger, A., Faix, J., Rivero, F. & Noegel, A.A. A Cdc42- and Rac-interactive binding (CRIB) domain mediates functions of coronin. *Proc Natl Acad Sci U S A* **111**, E25-33 (2014).

50. Swaminathan, K. *et al.* Coronin7 regulates WASP and SCAR through CRIB mediated interaction with Rac proteins. *Sci Rep* **5**, 14437 (2015).

51. Gerisch, G. *et al.* Mobile actin clusters and traveling waves in cells recovering from actin depolymerization. *Biophys J* **87**, 3493-3503 (2004).

52. Killich, T. *et al.* The locomotion, shape and pseudopodial dynamics of unstimulated Dictyostelium cells are not random. *J Cell Sci* **106 (Pt 4)**, 1005-1013 (1993).

53. Tweedy, L., Susanto, O. & Insall, R.H. Self-generated chemotactic gradients-cells steering themselves. *Curr Opin Cell Biol* **42**, 46-51 (2016).

Figure 1

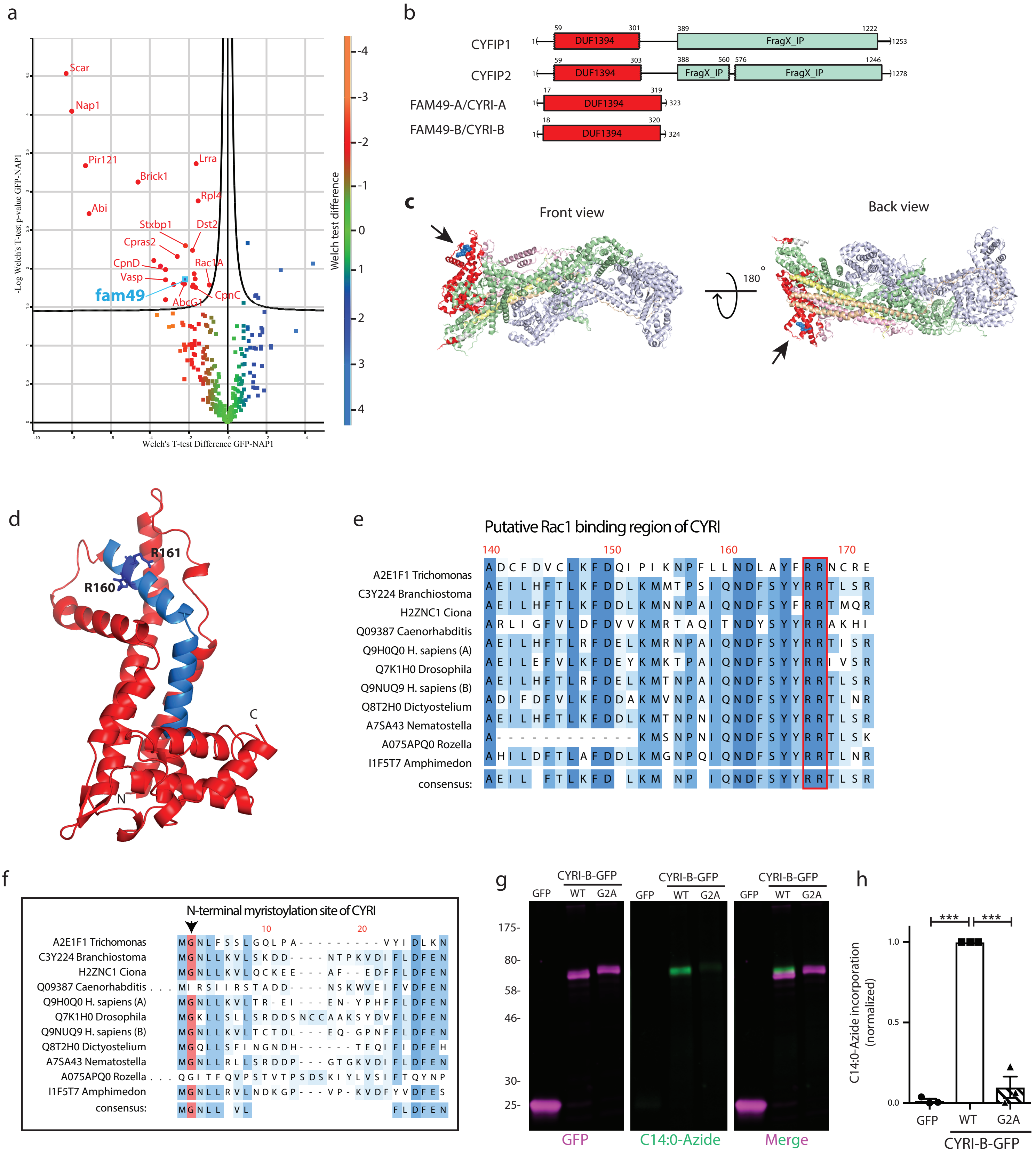
a
Scar
Nap1
Pir121
Brick1
Lrra
Rpl4
Abi
Stxbp1
Dst2
Cpras2
CpnD
Rac1A
Vasp
fam49
CpnC
AbcG1
-Log Welch's T-test p-value GFP-NAP1
Welch's T-test Difference GFP-NAP1
Welch test difference
-4
-3
-2
-1
0
1
2
3
4
b
CYFIP1
1
59
DUF1394
301
389
FragX_IP
1222
1253
CYFIP2
1
59
DUF1394
303
388
FragX_IP
560
576
FragX_IP
1246
1278
FAM49-A/CYRI-A
1
17
DUF1394
319
323
FAM49-B/CYRI-B
1
18
DUF1394
320
324
c
Front view
180 °
Back view
d
R161
R160
C
N
e
Putative Rac1 binding region of CYRI
140
150
160
170
A2E1F1 Trichomonas A D C F D V C L K F D Q I P I K N P F L L N D L A Y F R R N C R E
C3Y224 Branchiostoma A E I L H F T L K F D D L K M M T P S I Q N D F S Y Y R R T L S R
H2ZNC1 Ciona A E I L H F T L K F D D L K M N N P A I Q N D F S Y F R R T M Q R
Q09387 Caenorhabditis A R L I G F V L D F D V V K M R T A Q I T N D Y S Y Y R R A K H I
Q9H0Q0 H. sapiens (A) A E I L H F T L R F D E L K M R N P A I Q N D F S Y Y R R T I S R
Q7K1H0 Drosophila A E I L E F V L K F D E Y K M K T P A I Q N D F S Y Y R R I V S R
Q9NUQ9 H. sapiens (B) A E I L H F T L R F D E L K M T N P A I Q N D F S Y Y R R T L S R
Q8T2H0 Dictyostelium A D I F D F V L K F D D A K M V N P A I Q N D F S Y Y R R T L N R
A7SA43 Nematostella A E I L H F T L K F D D L K M T N P N I Q N D F S Y Y R R T L S R
A075APQ0 Rozella A - - - - - - - - - - - - K M S N P N I Q N D F S Y Y R R T L S K
I1F5T7 Amphimedon A H I L D F T L A F D D L K M G N P Q I Q N D F S Y Y R R T L N R
consensus: A E I L F T L K F D L K M N P I Q N D F S Y Y R R T L S R
f
N-terminal myristoylation site of CYRI
10
20
A2E1F1 Trichomonas M G N L F S S L G Q L P A - - - - - - - - - V Y I D L K N
C3Y224 Branchiostoma M G N L L K V L S K D D - - - - N T P K V D I F L D F E N
H2ZNC1 Ciona M G N L L K V L Q C K E E - - - A F - - E D F F L D F E N
Q09387 Caenorhabditis . . . M I R S I I R S T A D D - - - - N S K W V E I F V D F E N
Q9H0Q0 H. sapiens (A) M G N L L K V L T R - E I - - - E N - Y P H F F L D F E N
Q7K1H0 Drosophila M G K L L S L L S R D D S N C C A A K S Y D V F L D F E N
Q9NUQ9 H. sapiens (B) M G N L L K V L T C T D L - - - E Q - G P N F F L D F E N
Q8T2H0 Dictyostelium M G Q L L S F I N G N D H - - - - - - T E Q I F I D F E H
A7SA43 Nematostella M G N L L R L L S R D D P - - - G T G K V D I F L D F E N
A075APQ0 Rozella . . . Q G I T F Q V P S T V T P S D S K I Y L V S I F T Q Y N P
I1F5T7 Amphimedon M G N L L R V L N D K G P - - - V P - K V D F Y V D F E S
consensus: M G N L L V L F L D F E N
g
GFP
CYRI-B-GFP
WT
G2A
175-
80-
58-
46-
30-
25-
GFP
C14:0-Azide
Merge
h
***
***
C14:0-Azide incorporation (normalized)
1.0
0.5
0.0
GFP
WT
G2A
CYRI-B-GFP

Figure 2

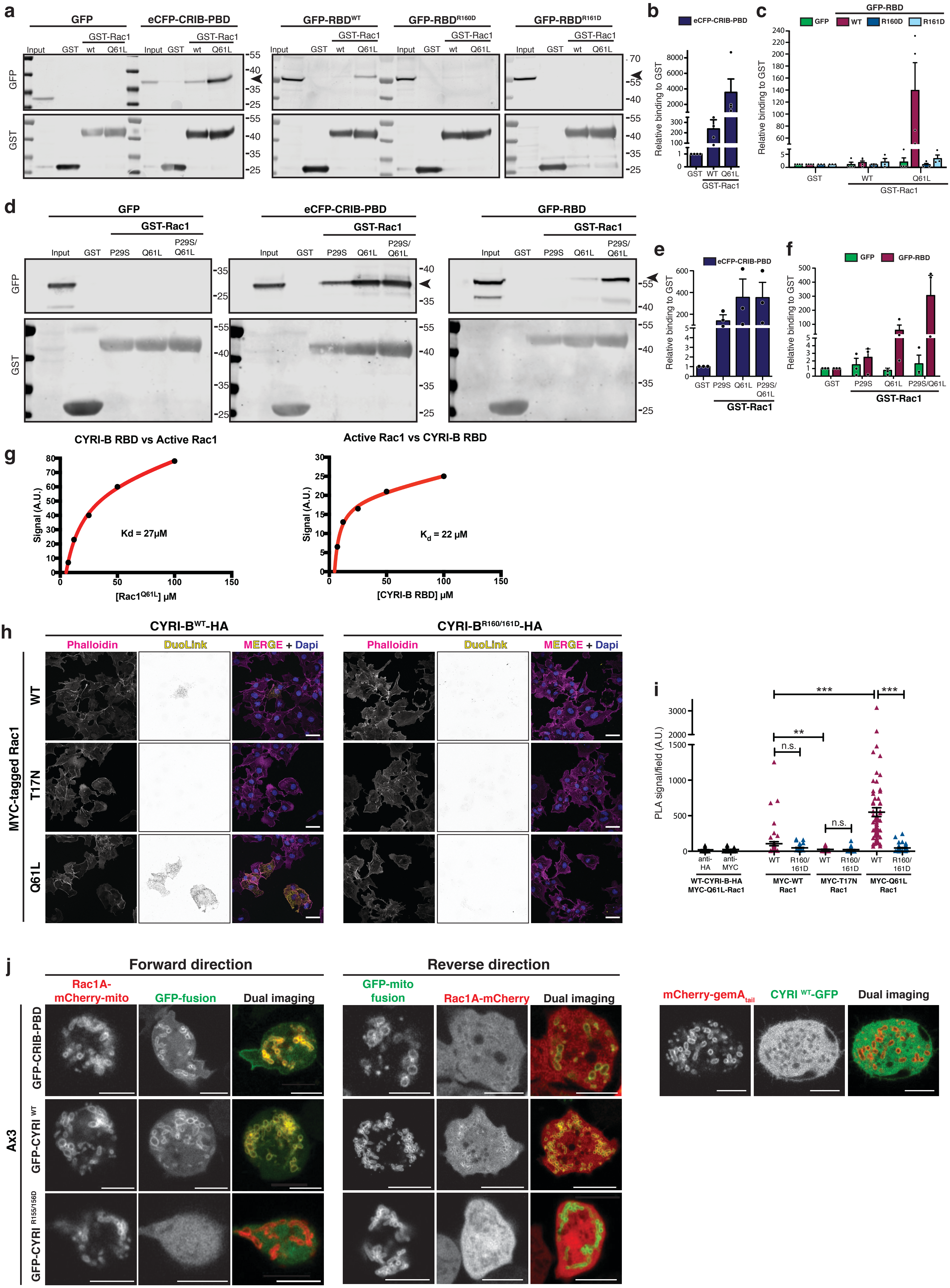
a
GFP
eCFP-CRIB-PBD
GFP-RBD^{WT}
GFP-RBD^{R160D}
GFP-RBD^{R161D}
GST-Rac1
Input GST wt Q61L
GFP
GST
55
40
35
25
70
b
eCFP-CRIB-PBD
Relative binding to GST
8000
6000
4000
2000
300
200
100
1
0
GST WT Q61L
GST-Rac1
c
GFP-RBD
GFP WT R160D R161D
Relative binding to GST
240
220
200
180
160
140
120
100
80
60
5
0
GST WT Q61L
GST-Rac1
d
GFP
eCFP-CRIB-PBD
GFP-RBD
GST-Rac1
Input GST P29S Q61L P29S/Q61L
GFP
GST
e
eCFP-CRIB-PBD
Relative binding to GST
600
400
200
5
4
3
2
1
0
GST P29S Q61L P29S/Q61L
GST-Rac1
f
GFP GFP-RBD
Relative binding to GST
500
400
300
200
100
5
4
3
2
1
0
GST P29S Q61L P29S/Q61L
GST-Rac1
g
CYRI-B RBD vs Active Rac1
Signal (A.U.)
Kd = 27μM
[Rac1^{Q61L}] μM
0 50 100 150
Active Rac1 vs CYRI-B RBD
Signal (A.U.)
K_d = 22 μM
[CYRI-B RBD] μM
0 50 100 150
h
CYRI-B^{WT}-HA
CYRI-B$^{R160/161D}$-HA
Phalloidin
DuoLink
MERGE + Dapi
MYC-tagged Rac1
WT
T17N
Q61L
i
PLA signal/field (A.U.)
3000
2000
1500
1000
500
0
***
***
**
n.s.
n.s.
anti-HA
anti-MYC
WT
R160/161D
WT-CYRI-B-HA
MYC-Q61L-Rac1
MYC-WT Rac1
MYC-T17N Rac1
MYC-Q61L Rac1
j
Forward direction
Reverse direction
Rac1A-mCherry-mito
GFP-fusion
Dual imaging
GFP-mito fusion
Rac1A-mCherry
mCherry-gemA$_{tail}$
CYRI ^{WT}-GFP
Ax3
GFP-CRIB-PBD
GFP-CYRI ^{WT}
GFP-CYRI $^{R155/156D}$

Figure 3

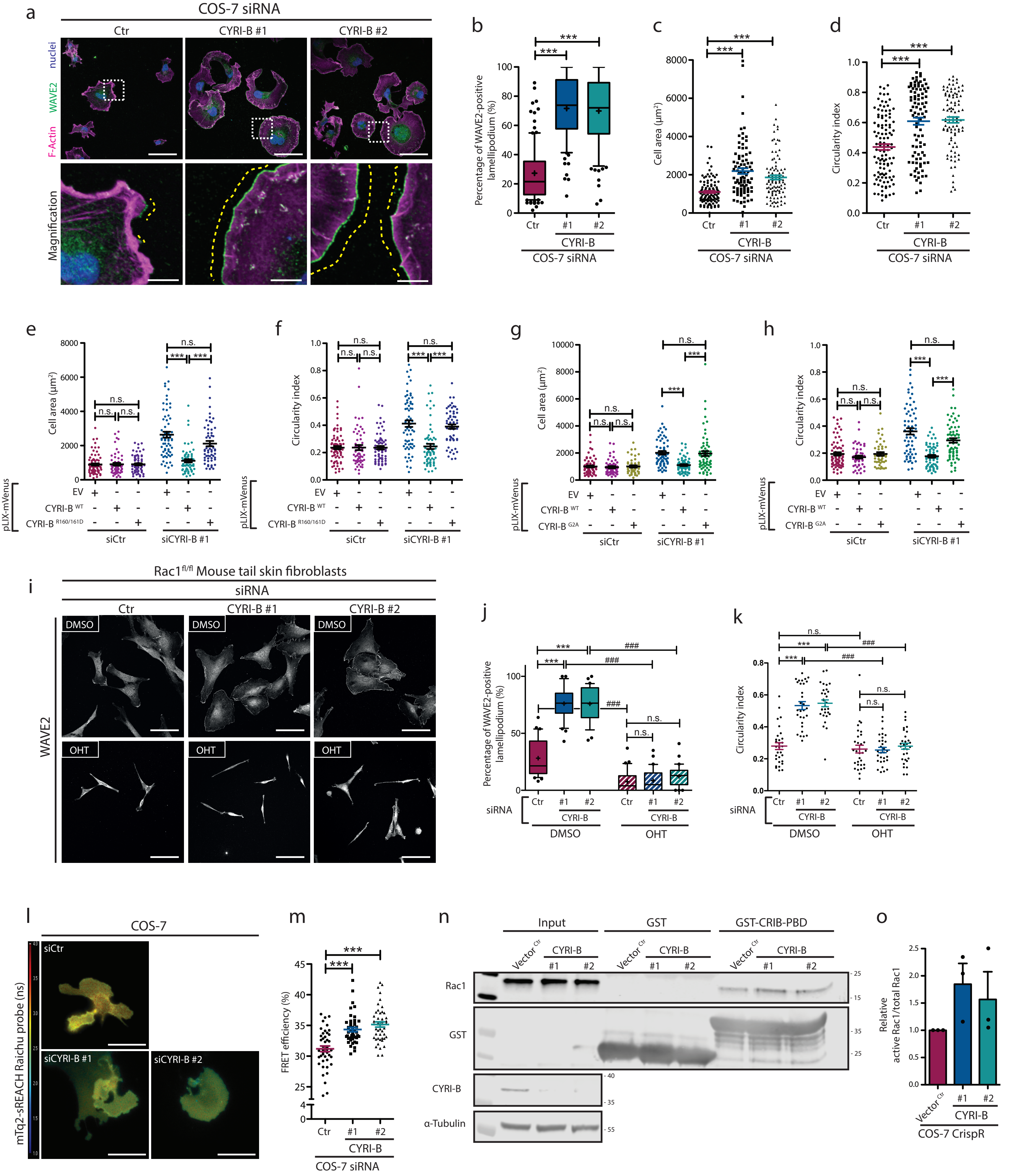
a
COS-7 siRNA
Ctr
CYRI-B #1
CYRI-B #2
nuclei
WAVE2
F-Actin
Magnification
b
Percentage of WAVE2-positive lamellipodium (%)
***
***
Ctr
#1
#2
CYRI-B
COS-7 siRNA
c
Cell area (µm²)
d
Circularity index
e
f
g
h
n.s.
EV
CYRI-B WT
CYRI-B R160/161D
CYRI-B G2A
pLIX-mVenus
siCtr
siCYRI-B #1
i
Rac1fl/fl Mouse tail skin fibroblasts
siRNA
WAVE2
DMSO
OHT
j
###
k
l
COS-7
siCtr
siCYRI-B #1
siCYRI-B #2
mTq2-sREACH Raichu probe (ns)
m
FRET efficiency (%)
n
Input
GST
GST-CRIB-PBD
Vector Ctr
Rac1
CYRI-B
α-Tubulin
o
Relative active Rac1/total Rac1
COS-7 CrispR

Figure 4

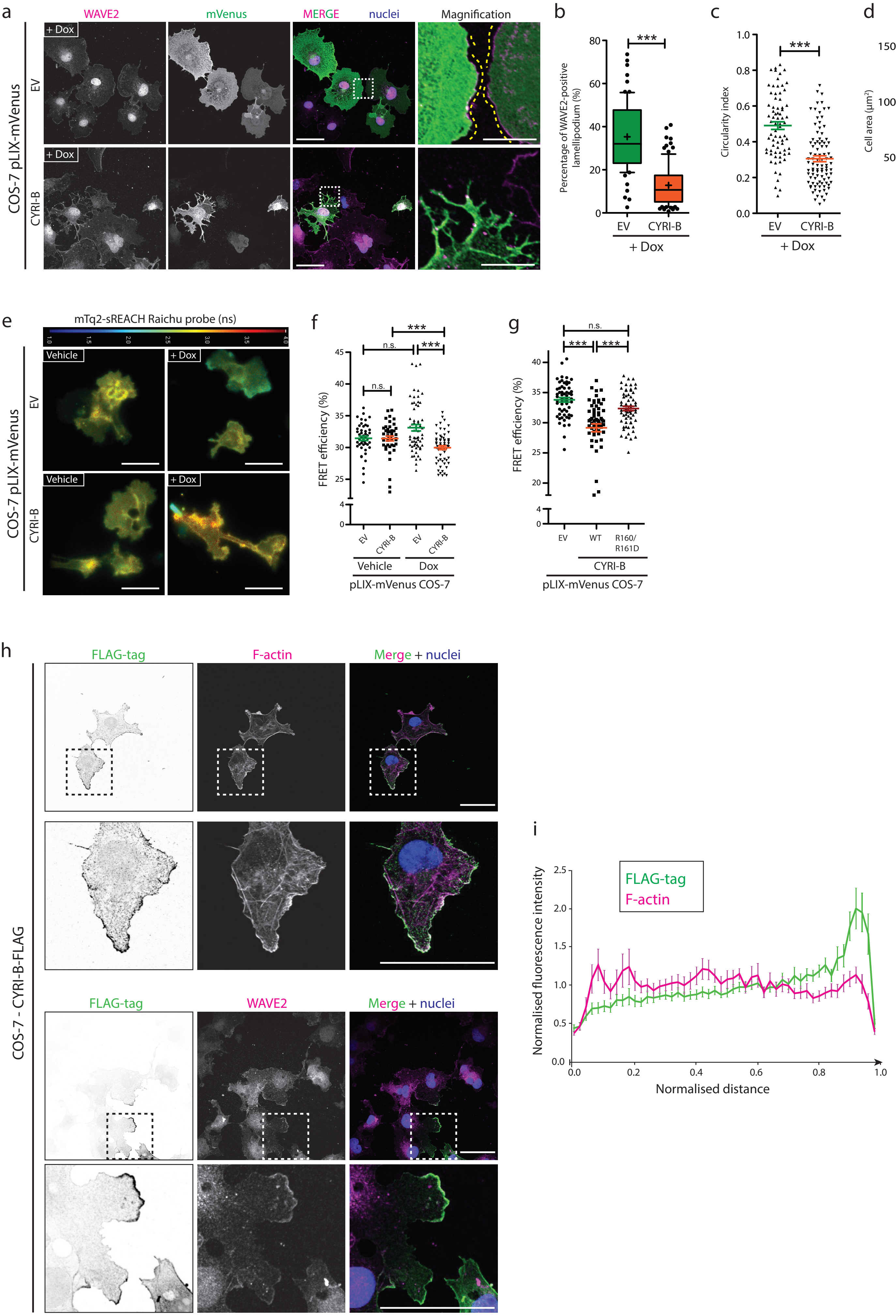
a
WAVE2
mVenus
MERGE
nuclei
Magnification
COS-7 pLIX-mVenus
EV
CYRI-B
+ Dox
+ Dox
b
Percentage of WAVE2-positive lamellipodium (%)
80
60
40
20
0
***
EV
CYRI-B
+ Dox
c
Circularity index
1.0
0.8
0.6
0.4
0.2
0.0
***
EV
CYRI-B
+ Dox
d
Cell area (µm²)
15000
10000
5000
0
***
EV
CYRI-B
+ Dox
e
mTq2-sREACH Raichu probe (ns)
1.0
1.5
2.0
2.5
3.0
3.5
4.0
COS-7 pLIX-mVenus
EV
CYRI-B
Vehicle
+ Dox
Vehicle
+ Dox
f
FRET efficiency (%)
45
40
35
30
25
4
0
n.s.
n.s.
***
***
EV
CYRI-B
EV
CYRI-B
Vehicle
Dox
pLIX-mVenus COS-7
g
FRET efficiency (%)
40
35
30
25
20
4
0
n.s.
***
***
EV
WT
R160/R161D
CYRI-B
pLIX-mVenus COS-7
h
FLAG-tag
F-actin
Merge + nuclei
FLAG-tag
WAVE2
Merge + nuclei
COS-7 - CYRI-B-FLAG
i
Normalised fluorescence intensity
2.5
2.0
1.5
1.0
0.5
0.0
0.0
0.2
0.4
0.6
0.8
1.0
Normalised distance
FLAG-tag
F-actin

Figure 5

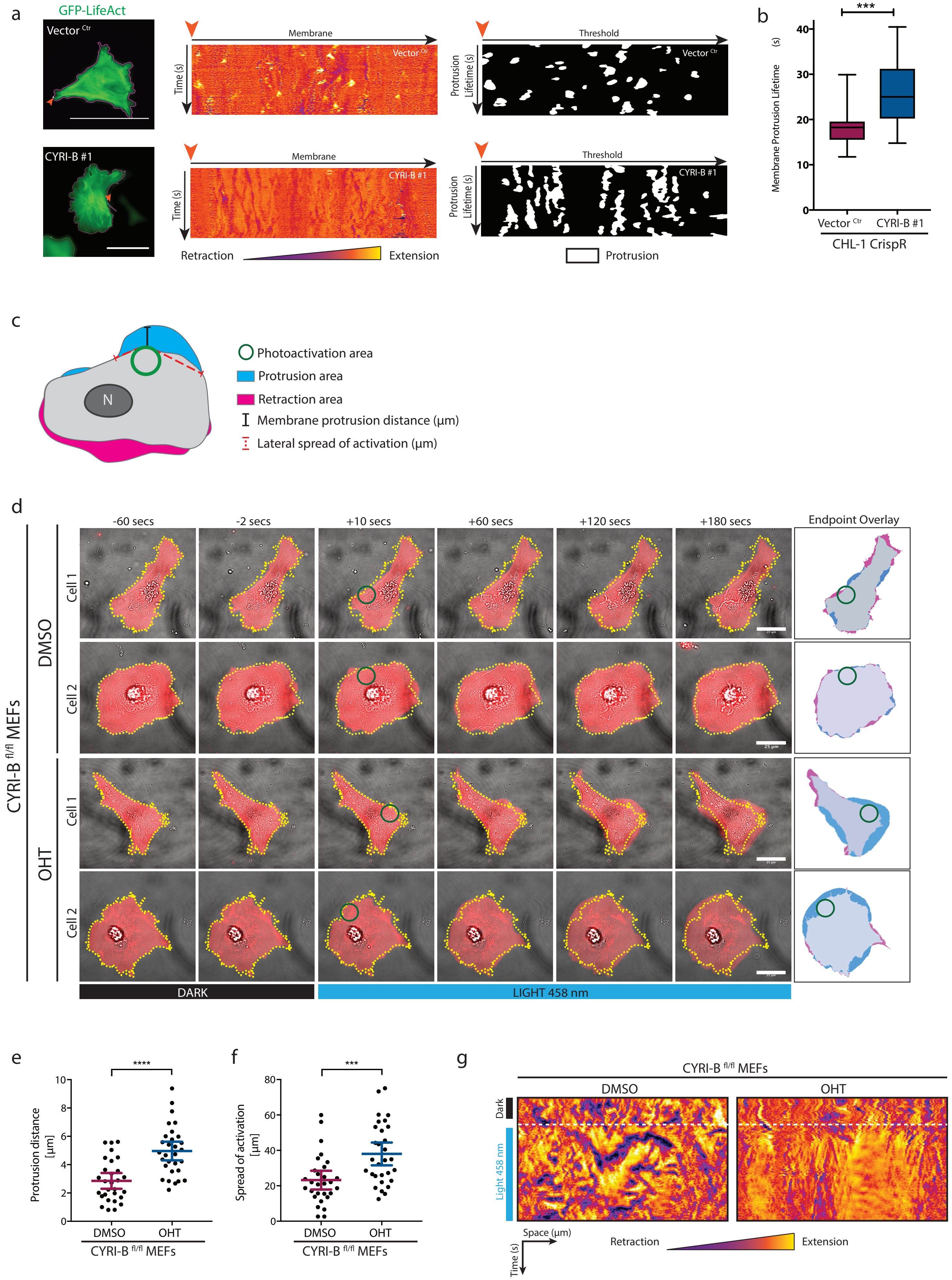

a
GFP-LifeAct
Vector Ctr
CYRI-B #1
Membrane
Time (s)
Vector Ctr
CYRI-B #1
Retraction
Extension
Threshold
Protrusion Lifetime (s)
Protrusion
b
***
Membrane Protrusion Lifetime (s)
40
30
20
10
0
Vector Ctr
CYRI-B #1
CHL-1 CrispR
c
N
Photoactivation area
Protrusion area
Retraction area
Membrane protrusion distance (µm)
Lateral spread of activation (µm)
d
-60 secs
-2 secs
+10 secs
+60 secs
+120 secs
+180 secs
Endpoint Overlay
CYRI-B fl/fl MEFs
DMSO
OHT
Cell 1
Cell 2
DARK
LIGHT 458 nm
e
****
Protrusion distance [µm]
10
8
6
4
2
0
DMSO
OHT
CYRI-B fl/fl MEFs
f
***
Spread of activation [µm]
80
60
40
20
0
DMSO
OHT
CYRI-B fl/fl MEFs
g
CYRI-B fl/fl MEFs
DMSO
OHT
Dark
Light 458 nm
Space (µm)
Time (s)
Retraction
Extension

Figure 6

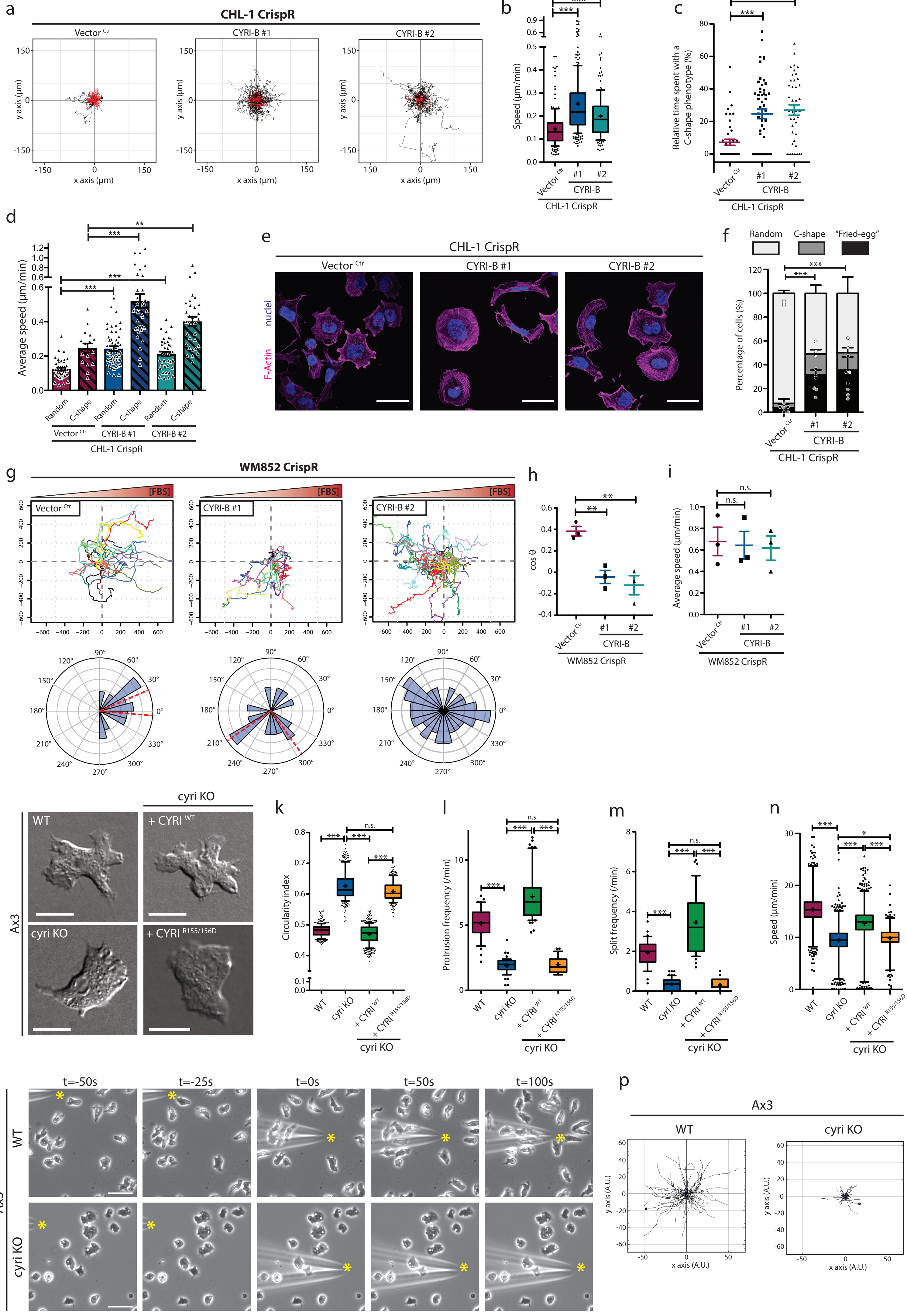
a
CHL-1 CrispR
Vector Ctr
CYRI-B #1
CYRI-B #2
y axis (µm)
x axis (µm)
150
0
-150
b
Speed (µm/min)
***
Vector Ctr
#1
#2
CYRI-B
CHL-1 CrispR
c
Relative time spent with a C-shape phenotype (%)
***
d
Average speed (µm/min)
**
Random
C-shape
Vector Ctr
CYRI-B #1
CYRI-B #2
CHL-1 CrispR
e
CHL-1 CrispR
Vector Ctr
CYRI-B #1
CYRI-B #2
nuclei
F-Actin
f
Random
C-shape
"Fried-egg"
Percentage of cells (%)
g
WM852 CrispR
[FBS]
Vector Ctr
CYRI-B #1
CYRI-B #2
90°
60°
30°
0°
330°
300°
270°
240°
210°
180°
150°
120°
h
cos θ
**
Vector Ctr
#1
#2
CYRI-B
WM852 CrispR
i
Average speed (µm/min)
n.s.
j
cyri KO
WT
+ CYRI WT
cyri KO
+ CYRI R155/156D
Ax3
k
Circularity index
***
n.s.
WT
cyri KO
+ CYRI WT
+ CYRI R155/156D
cyri KO
l
Protrusion frequency (/min)
m
Split frequency (/min)
n
Speed (µm/min)
*
o
t=-50s
t=-25s
t=0s
t=50s
t=100s
WT
cyri KO
Ax3
p
Ax3
WT
cyri KO
y axis (A.U.)
x axis (A.U.)

Figure 7

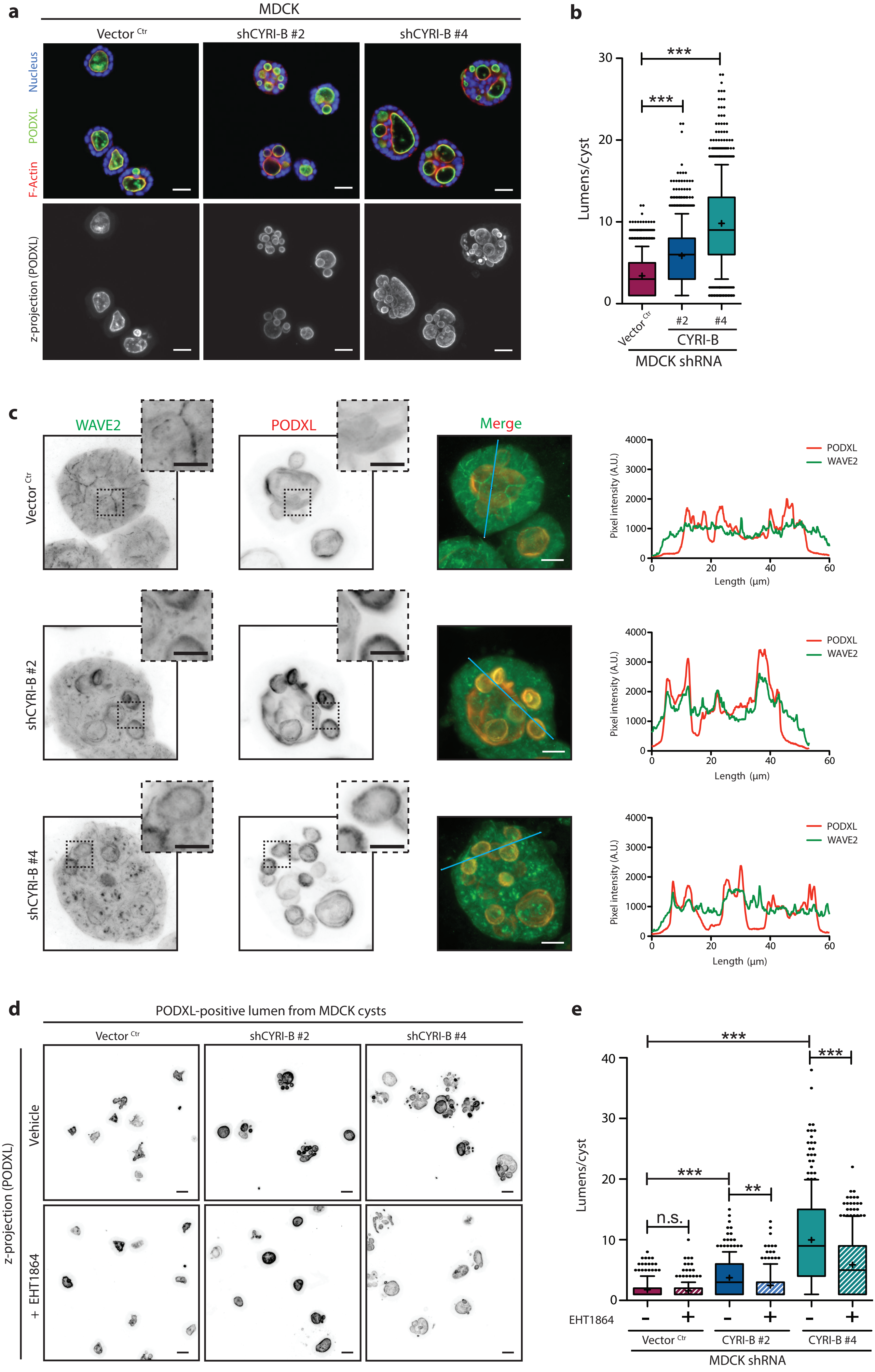
a
MDCK
Vector Ctr
shCYRI-B #2
shCYRI-B #4
Nucleus
PODXL
F-Actin
z-projection (PODXL)
b
***
***
Lumens/cyst
30
20
10
0
Vector Ctr
#2
#4
CYRI-B
MDCK shRNA
c
WAVE2
PODXL
Merge
Vector Ctr
shCYRI-B #2
shCYRI-B #4
Pixel intensity (A.U.)
4000
3000
2000
1000
0
20
40
60
Length (µm)
PODXL
WAVE2
d
PODXL-positive lumen from MDCK cysts
Vector Ctr
shCYRI-B #2
shCYRI-B #4
Vehicle
+ EHT1864
z-projection (PODXL)
e
***
***
***
**
n.s.
Lumens/cyst
40
30
20
10
0
EHT1864
-
+
-
+
-
+
Vector Ctr
CYRI-B #2
CYRI-B #4
MDCK shRNA

Methods

Antibodies and constructs

Antibodies and DNA constructs are listed in Supplementary Tables 3 and 4 respectively.

Alignment and phylogenetic tree

Protein sequences were obtained from Uniprot http://www.uniprot.org/ and aligned using MacVector software. The phylogenetic tree was constructed based on the major eukaryotic superclasses as previously defined[14] and based on previous identification of Arp2/3 complex and Scar/WAVE complex sequences[15, 54]. BLAST homology search on the NCBI website https://blast.ncbi.nlm.nih.gov/Blast.cgi. *Dictyostelium*, human or a close relative were searched against the complete translated genome of open reading frames from these organisms.
HMM logo was generated by feeding the Pfam database of the DUF1394 domain into Skylign[55].

CYRI-B structure prediction

The predicted protein structure of CYRI-$B_{31\text{-}292}$ was generated by the protein homology/analogy recognition engine (Phyre)[56] using the cytoplasmic fmr1-interacting protein 1 (PDB 3P8C) as a template with 100% homology confidence and 18% sequence identity.

Mammalian cell lines and growth conditions

CHL-1, HEK293T, COS-7 cells were maintained in Dulbecco's Modified Eagle's Medium supplemented with 10% FBS and 2 mM L-Glutamine (DMEM).
ROSA26:CreER$^{t2+;}$ *Ink4*$^{-/-}$*Cyri-B*$^{wt/wt}$; *Rac1*$^{fl/fl}$ mouse tail skin fibroblasts and ROSA26:CreER$^{t2+;}$*Ink4*$^{-/-}$; ***Cyri-B***$^{fl/fl}$ mouse embryonic fibroblasts were maintained in DMEM complemented with 1 mg/mL of primocin.
COS-7 cells transfected with the doxycycline-inducible system were grown in 10% tetracyclin-free FBS (ClonTech) and treated with 5 µg/mL doxycycline for 48h.
MDCK cells were maintained in 5% FBS and 2 mM L-Glutamine supplemented minimum essential medium, high glucose, high sodium bicarbonate.
WM852 cells were grown in RPMI supplemented with 10% FBS and 2 mM L-Glutamine.
All mammalian cell lines used in this study were maintained in 10 cm plastic dishes at 37 °C and 5% CO_2.
Cell lines were regularly tested for mycoplasma contamination (MycoAlert - Lonza).

CLICK Chemistry of Mammalian CYRI-B

HEK293T cells plated on 24-well plate were transfected with 1 µg of pEGFPN1 or CYRI-B-EGFP (wild-type or G2A mutant) using Lipofectamine 2000 and were processed the next day. C14:0-azide was synthesised as previously described[57]. Transfected HEK293T cells were incubated with 100 µM of C14:0-azide (in DMEM with 1 mg/mL defatted BSA) for 4 h at 37 °C. Cells were washed twice in PBS and lysed on ice for 10 min in 100 µL lysis buffer (150 mM NaCl, 1 % Triton X-100, 50 mM Tris-HCl, pH 8.0, containing protease inhibitors). Cell lysates were centrifuged at 10000 x g for 10 min at 4 °C to remove cell debris. Alkyne IR-800 Dye to C14:0 azide was conjugated for 1 h at room temperature (RT) with end-over-end rotation by adding an equal volume of freshly mixed click chemistry reaction mixture (10 µM 800 CW alkyne infrared dye, 4 mM CuSO4, 400 µM Tris[(1-benzyl-1H-1,2,3-triazol-4-yl)methyl]amine, and 8 mM ascorbic acid in dH_20) to the supernatants. GFP-tagged proteins were isolated using the µMACS GFP isolation kit following manufacturer's protocol and resolved by SDS-PAGE as described below. Protein acylation was quantified by expressing the intensity of the CLICK signal relative to the protein signal.

Yeast Two-Hybrid screen

Screening was performed at Hybrigenics services *as per* their standard protocols. Briefly, the coding sequence for the constitutively active full-length Rac1 (NM_006908.4 ; mutations G12V, C189S) was PCR-amplified and cloned into pB27 as a C-terminal fusion to LexA (LexA-Rac1). All libraries use the prey vector pP6. pB27 and pP6 are derived from the original pBTM116[58] and pGADGH[59] plasmids, respectively.

The bait was screened against the different libraries using a mating approach with YHGX13 (Y187 ade2-101::loxP-kanMX-loxP, mat alpha) and L40deltaGal4 (mat-a) yeast strains as previously described[60]. Positive colonies were selected on a medium lacking tryptophan, leucine and histidine, and supplemented with 3-aminotriazole. The prey fragments of the positive clones were amplified by PCR and sequenced at their 5' and 3' junctions. Interacting proteins were identified in the GenBank database (NCBI).

GST Pull-down of Mammalian CYRI-B and GTPases

DH5alpha *E. coli* cells were grown at OD_{600nm} 0.4 and induced for 4h with 0.2 mM IPTG. Pellet was resuspended in ice-cold buffer A (50 mM NaCl, 50 mM Tris-HCl pH 7.5, 5 mM $MgCl_2$, 3 mM DTT) and sonicated, followed by a 30 min spin at 20000 rpm to yield lysate. GST tagged proteins were immobilized on pre-washed glutathione-sepharose beads for 30 min at 4°C with gentle agitation and unbound proteins were washed out 3 times in buffer A.

Cells transfected with GFP constructs were collected in ice-cold lysis buffer (100 mM NaCl, 25 mM Tris-HCl pH 7.5, 5 mM $MgCl_2$, 1X protease and phosphatase inhibitors, 0.5% NP-40). 1.5-2 mg of proteins were mixed with pre-equilibrated beads with gentle agitation during 2h at 4°C. Beads were then washed 3 times in washing buffer (100 mM NaCl, 25 mM Tris-HCl pH 7.5, 5 mM $MgCl_2$), resuspended in sample buffer containing DTT and resolved by SDS-PAGE as described below.

MBP Pull-down

Recombinant proteins were purified as mentioned above and immobilized on MBP-trap beads. Beads were mixed with similar amount of recombinant GST-tagged proteins in ice-cold buffer A (see above) containing 0.05% Triton X100. Binding was allowed for 2h at 4°C and beads were then thoroughly washed in ice-cold buffer A. Proteins were eluted by adding boiling sample buffer directly to the beads and prepared for SDS-PAGE.

Mutagenesis of Mammalian CYRI-B

Point mutation was inserted using the Q5-site directed kit (New England Biolabs) and following the manufacturer's instructions. Primers were designed using NEBaseChanger - see Supplementary Table 5.

Protein purification for SPR analysis

E. Coli BL21 CodonPlus (DE3)-RIL (Agilent Tech.) and *E. Coli* BL21 (DE3) pLysS (Promega) were used for GST-tagged and His-Tagged proteins respectively.
Pre-culture was grown overnight in L-Broth (LB) containing appropriate antibiotics. Once reaching OD_{600nm} 0.4, protein expression was induced using 0.2 mM IPTG and culture was kept overnight at 20°C under agitation (200 rpm). Cells were lysed in Buffer 1 (200 mM NaCl, 30 mM Tris-HCl pH 7.5, 5 mM $MgCl_2$, 3 mM β-mercaptoethanol) containing protease inhibitors and passed through a 20,000 psi-pressurised microfluidizer. The soluble fraction was collected by centrifugation (30 min, 20000 rpm) and loaded onto an equilibrated GSTrap HP or HisTrap HP column using an AKTA machine (GE Healthcare). Proteins were either directly eluted using Buffer 1 containing either 20 mM GSH for GST-tagged proteins or 300 mM Imidazole pH 7.5 for His-tagged proteins. Cleavage on the column was performed overnight with the appropriate protease, flowing at 0.1 ml/min in a loop connected to the AKTA machine. Proteins were gel purified (HiLoad 16/600 Superdrex 75pg or HiLoad 16/600 Superdrex 200pg) in Buffer 2 (150 mM NaCl, 25 mM Tris-HCl pH 7.5, 5 mM $MgCl_2$, 2 mM β-mercaptoethanol), snap-frozen and stored at -80°C.

Surface Plasmon Resonance (SPR) protein binding assay

SPR analysis was performed using Biacore T200 (GE Healthcare) equilibrated with buffer 2 (see above) supplemented with 0.5% of surfactant P20. GST-tagged proteins were immobilised at 22°C onto CM5 sensor chip functionalized with anti-GST and reached ~320 RU. Same procedure was used for His-tagged protein onto NTA sensor chip and reached 650 RU. All immobilisation steps were done at a flow rate of 10 µL/min. Serial dilution of each analyte was injected across a reference flow cell and the flow cell containing the ligand at a flow rate of 30 µL/min. Data were solvent corrected, reference subtracted, quality controlled and evaluated using the Biacore T200 evaluation software. Affinity was determined by curve fitting a 1:1 binding model.

Proximity ligation assay

COS-7 cells expressing CYRI-B-HA and MYC-Rac1 constructs were plated on laminin-coated coverslips and used for DuoLink *in situ* proximity ligation assay (Sigma - mouse and rabbit - Red detection) using the manufacturer's protocol. Mouse anti-HA (Covance) and Rabbit anti-MYC-tag (CST) were used at 1:400 and 1:200 respectively. Incubation with either antibody was performed as a negative control.

Enforced mitochondrial localisation

The Rac1A cDNA (gift of A. Kortholt, University of Groningen) was mutagenised to

P29S/Q61L the stop codon removed. It was cloned N-terminal to mCherry-mitochondrial anchor, or N-terminal to mCherry to give a cytosolic version. Likewise, PakB-CRIB was cloned N-terminal to either GFP alone (to give a soluble CRIB fusion) or GFP-mito (to give a mitochondrial-targeted version). CYRI was similarly used in its WT or R155D R156D double mutant. The mitochondrial anchor consists of the C-terminal tail (aa 602-658) of gemA, the *Dictyostelium* mitochondrial-anchored Rho1/2 GTPases.

Live cell images were acquired at separate times using single-channel hardware setups to ensure zero channel bleed-through or dual excitation of fluorophores. To note, the cells move between image captures. Dual images were captured using a double band-pass filter that allows both red and green signals to pass simultaneously. The same cells are shown in the red, green and dual images.

Transfection, siRNA Treatment and Knockout Mammalian Cells.

Oligos used are listed in Supplementary Table 5.

Cells were plated a day before transfection at 70% of confluence and later transfected using Lipofectamine 2000 according to the manufacturer's instructions. 2-5 µg of DNA was used per reaction based on a 6-well plate format.

siRNA oligonucleotides targeting CYRI-B (Qiagen): Mouse tail fibroblasts and COS-7 cells were respectively treated with 75 nM of *Mus musculus* CYRI-B siRNA and 25 nM of *Homo sapiens* CYRI-B siRNA (recognised *Cercopithecus aethiops)* or matched concentration of control siRNA (AllStars Negative siRNA – Qiagen) were transfected using Lullaby transfection reagent according to manufacturer's instructions. The same step was repeated 48h later and cells were analysed after 24h.

For CrispR/Cas9 mediated knock out, sgRNA were selected using the MIT CrispR designing tool (http://crispr.mit.edu/). Annealed oligonucleotides were cloned into pLentiCrispRv2-Puro. Briefly, HEK293T cells were seeded at 1.5 x 10^6 cells/10cm dish. Cells were transfected with 10 µg of the selected plasmid (Vector ^{Ctr} or containing a gRNA against CYRI-B) 7.5 µg of pSPAX2 (Addgene 8454) and 4 µg of pVSVG (Addgene 12260) in a final volume of 440 µL of sterile water, and complemented with 500 µL 2X HBS and 120 mM $CaCl_2$. Solution was incubated 30 min at 37°C before adding to HEK293T cells. Medium was removed after 24h and replaced by 6 mL of 20 % FBS DMEM. Meanwhile, recipient cells were plated at 1 x 10^6 cells/10cm dish. The day after, supernatants were filtered through a 0.45 µm pore membrane and mixed with 25 µg of hexadimethrine bromide (4.2 µg/mL final) before infecting recipient cells. Infection was repeated the next day and stably transfected cells were selected with 1 µg/mL of puromycin.

Same procedure was used for lentiviral infection of the MDCK cells and cells were selected with 5 µg/mL of puromycin.

For CrispR COS-7 *cyri-b* knockout cells, human gRNAs against *CYRI-B* (CrispR#1 or #2 - See Table 5) were cloned into a pSpCas9(BB)-2A-GFP vector (Addgene plasmid #48138) using the restriction enzyme B*bsI* as described in[61] COS-7 cells were seeded onto 6 cm dishes and transfected the day after using Lipofectamine

2000 with 5 μg of pSpCas9(BB)-2A-GFP (empty vector or *CYRI-B* targeting CrispR gRNA) following the manufacturers guidelines. Cells were grown for approximately 24 h before FACS sorting. The transfected cells were trypsinised, resuspended in serum free DMEM with DAPI (1 μg/ml) and filtered through a 0.45 μm pore membrane for FACS. For FACS, gates were drawn to sort by cell size, live/dead and GFP positive cells. GFP positive sorted cells were incubated with DMEM complete and left to grow at normal culturing conditions. Knockouts for *CYRI-B* were analysed by western blotting.

Generation of knockout mouse embryonic fibroblast and mouse tail skin fibroblast cell lines were obtained by adding 1 μM of hydroxytamoxifen in the growth medium every 3 days over 7 days.

FRET imaging of Mammalian Cells

The Rac1-Raichu-mTq2-sREACH probe is described in[29]. Cells were transfected with the probe, plated the day after on laminin and imaged. FRET images were acquired with the Nikon FLIM/TIRFsystem Z6014 microscope equipped with a Plan Apochromat 63x/1.45 oil objective and a 465 nm LED. Dishes were placed in a 37°C heated chamber perfused with 5% CO_2. FRET efficiency was calculated by standardizing the probe lifetime to the average lifetime of the donor alone as follows:

$$FRET\ efficiency\ (\%) = \frac{Average\ lifetime\ donor - Lifetime\ probe}{Average\ lifetime\ donor}\ x100$$

Active Rac1 pulldown

COS-7 cells were plated on laminin-coated dishes for 1h, washed twice with ice-cold PBS and lysed using 50 mM Tris-HCl pH 7.4, 500 mM NaCl, 1% Triton X-100, 0.5% sodium deoxycholate, 10 mM $MgCl_2$, 1X protease and phosphatase inhibitors. Cleared lysates were incubated with recombinant GST or GST-CRIB-PBD obtained from DH5alpha cells as described above. 1-1.5 mg of lysate were incubated for 2 h at 4°C with a similar amount of GST-construct immobilised on glutathion-sepharose beads. Beads were washed 3 times with 50 mM Tris-HCl pH 7.4, 500 mM NaCl, 10 mM $MgCl_2$ and prepared for SDS-PAGE analysis as described below.

SDS-PAGE and Western Blotting of Mammalian Cells

Lysates were collected on ice by scraping cells in RIPA Buffer (150 mM NaCl, 10 mM Tris-HCl pH 7.5, 1 mM EDTA, 1% Triton X100, 0.1% SDS, 1X protease and phosphatase inhibitors) and centrifuged 10 min at 15000 rpm and 4°C. Protein concentration was measured at OD_{600nm} using Precision Red.

20-40 μg of protein were resolved on a NuPAGE Novex 4-12% Bis-Tris gels and transferred onto a nitrocellulose membrane using the BioRad system. Membranes were blocked in 5% non-fat milk in TBS-T (10 mM Tris pH 8.0, 150 mM NaCl, 0.5% Tween 20) during 30 min before overnight incubation with primary antibodies at 4°C. Membranes were washed 3x 5 min in TBS-T and incubated 1h with Alexa-Fluor conjugated secondary antibodies. Blots were then washed 3x 5 min and imaged using the LiCor Odyssey CLx.

All images were then analysed using Image StudioLite v.5.2.5.

Immunofluorescence of Mammalian Cells

Cells were collected and plated onto sterile 13mm glass coverslips coated overnight at 4°C with 10 µg/mL of rat-tail collagen I, 10 µg/mL fibronectin or 10 µg/mL laminin diluted in PBS. Coverslip were washed 3x in PBS before seeding cells. Cells were fixed with 4% paraformaldehyde for 10 min, permeabilised (20 mM Glycine, 0.05% Triton X100) for 10 min and blocked with 5% BSA-PBS for 30 min. Primary and secondary antibodies were diluted in blocking buffer and incubated 1h in a dark and humidified chamber. Coverslips were washed twice in PBS and once in water before being mounted on glass slides using ProLong Gold antifade reagent. Images were taken using an inverted Olympus FV1000 confocal microscope using a Plan Apochromat N 63x/1.40 oil SC or an Uplan FL N 40x/1.30 oil objective.

Images were processed and analysed using Fiji software (ImageJ v1.48t)[16].

Membrane dynamics analysis

CHL-1 cells were transfected with GFP-LifeAct (5 µg AMAXA kit-T, program T-020) and incubated overnight in complete DMEM. Cells were then plated onto a glass bottom dish coated with laminin for 3 h before imaging within a contained unit at 37°C and 5% CO_2. Time-lapse images were taken using a Nikon microscope with a CoolLED GFP filter set (470 nm LED) and a Nikon Plan Apo VC 100x/1.4 NA oil immersion objective and captured using a Photometrics PRIME camera. GFP images were taken at 1 frame per second for a total of 3 min. For each frame, a binary mask was made of the cell based on the intensity of its LifeAct signal, and the intensity of an associated edge image made by Canny edge detection. Differences between binary images from one frame to the next were used to find areas of extension or retraction, with extended areas positively valued and retracted areas negatively valued. Co-ordinates for an outline of the binary image of each frame were extracted from the ROI class in ImageJ, and were used to measure the mean intensity of the corresponding difference image in a 5x5 px area. These values were then written for each cell to a new 2D image that we refer to as an "unwrapped kymograph", with each two rows representing one frame and each column representing one outline coordinate point for that frame. After smoothing this unwrapped kymograph, areas of protrusion were identified by thresholding, with their extension in the y direction (time) measured. This gave us an estimate of the active lifetime of each protrusion, and a mean protrusion lifetime for each cell. Images were processed using Metamorph and Fiji softwares.

Plugin used for creating kymograph will be provided upon reasonable request.

Rac1 photo activation

Transfection protocol: MEFs were transiently transfected by electroporation (Amaxa kit T) with 5 µg of photoactivatable Rac1 plasmid[31] (pTriEx-LOV2-Ja-Rac1-mCherry). The transfected cells were suspended in complete DMEM media, and plated onto laminin-coated glass-bottom 35 mm dishes. After several hours, the media was replaced with serum-free DMEM and incubated overnight in darkness.

Imaging: Imaging was performed on a Zeiss 880 confocal microscope with a stage incubator perfused with CO_2. Time-lapse imaging of moderate mCherry expressing cells was done for 150 frames at 2 second intervals between frames. Two images were collected for each frame at 568 nm with bi-directional scanning averaged over two frames to image the mCherry tag, and a transmitted light detector to show a bright field image of the cell morphology, both at 1024x1024 resolution. An initial 29 frames (1 minute) was collected with 568 nm excitation to document baseline protrusive activity. Photoactivation of Rac1 was started at frame 30, and continued for each frame to 150, with a pulse of 458 nm excitation in a 100 pixel diameter region of interest. The 568 nm excitation was at 7.5% laser power, with gain of 600-800 depending on the brightness of the cell, and the pinhole set at 300 to maximize collection of light levels and depth of field to capture ruffles. The 458 nm excitation used laser power of 10% and scan speed set for a pixel dwell time of 8 µsec.

Movies were processed using the Plugin found in Supplementary Note 1

Chemotaxis assay

Chemotaxis assays with WM852 human melanoma cells were performed as described in[35]. Briefly 8 x 10^4 cells were seeded onto fibronectin coated coverslips and left overnight in serum-free RPMI. Coverslips were mounted onto Insall chambers with RPMI containing 10% fetal bovine serum as the chemoattractant, and images were taken every 15 min for 48 h with a Nikon TE2000-E time-lapse microscope using Metamorph software. Cells were manually tracked using MTrackJ plugin in Fiji. All cells that moved independently of other cells were chosen for tracking. Approximately 120 cells were tracked for each condition from 3 independent repeats per condition (see also legend Figure 6).

Random Migration Assay for Mammalian Cells

6-well glass bottom plates were coated overnight as described above. $1x10^5$ cells were plated and imaged every 10 min for 17 h using a Nikon TE2000 microscope, PlanFluor 10x/0.30 objective and equipped with a heated CO_2 chamber. Images were analysed using Fiji software[63] (ImageJ v1.48t). Individual cells were tracked using the mTrackJ plugin, and spider plots were generated using the chemotaxis and migration tool plugin (v.1.01).

Dictyostelium discoideum Cells

Axenic *D. discoideum* strains Ax3 was used as wildtype. *cyri* knockout cells were generated in Ax3 genetic backgrounds. Ax3-derived *napA* KO cells are described previously[64]. Cells were grown in HL5 medium (Formedium) with 100 U/ml penicillin and 100 µg/ml streptomycin in 10 cm plastic Petri dishes and incubated at 21°C.

Dictyostelium discoideum GFP-Trap with Formaldehyde Crosslinking

Cells were collected in PBS and lysed by adding ice-cold 3x lysis/crosslinking buffer (1x buffer: 20 mM HEPES pH 7.4, 2 mM $MgCl_2$, 3% formaldehyde, 0.2% Triton X-100). After 5 min with gentle agitation at 4 °C, formaldehyde was quenched for

10min on ice using 1.75 M Tris pH 8.0. Samples were centrifuged at 22000g for 4 min at 4 °C. Pellet was successively washed and resuspended with 1 mL of ice cold quenching buffer (0.4 M Tris pH 8.0, 0.2% Triton X-100), wash buffer A (100 mM HEPES pH 7.4, 2 mM $MgCl_2$, 0.2% Triton X-100) and wash buffer B (100 mM HEPES pH 7.4, 2 mM $MgCl_2$), with 3 min centrifugation step between washes. Final resuspension was performed using 1mL of ice-cold RIPA buffer (50 mM Tris-HCl pH 8.0, 150 mM NaCl, 0.5% Triton X-100, 0.5% sodium deoxycholate, 0.15% SDS, 5 mM EDTA, 2 mM DTT) and incubated 1h at 4 °C with gentle agitation. Supernatants were mixed with pre-equilibrated GFP-Trap beads (Chromotek) following manufacturer's protocol. Beads were washed 3x with 50 mM Tris-HCl pH 8.0, 150 mM NaCl, 5 mM EDTA followed by 1 wash with 10 mM Tris-HCl pH 8.0. Samples were eluted after incubation with 2x SDS loading buffer and heating 10 min at 70°C before loading on a SDS-PAGE.

Dictyostelium discoideum **GFP-NAP1 'in gel' Proteolytic Digestion – Mass Spectrometry Analysis**

Eluates from GFP-NAP1 immunoprecipitation were separated by SDS-PAGE and stained with Coomassie blue. Each gel lane was divided in 6 slices and digested[65]. Tryptic peptides from in gel digestions were separated by nanoscale C_{18} reverse-phase liquid chromatography using an EASY-nLC II (Thermo Fisher Scientific) coupled online to a Linear Trap Quadrupole - Orbitrap Velos mass spectrometer (Thermo Scientific) and desalted using a pre-column C18 NS-MP-10 100µm i.d. x 0.2 cm of length (NanoSeparations). Elution was at a flow of 300 nl/min over a 90 min gradient, into an analytical column C18 NS-AC-11 75µm i.d. x 15 cm of length (NanoSeparations). For the full scan a resolution of 30,000 at 400 Th was used. The top ten most intense ions were selected for fragmentation in the linear ion trap using Collision Induced Dissociation using a maximum injection time of 25 ms or a target value of 5000 ions. MS data were acquired using the XCalibur software (Thermo Fisher Scientific).

Raw data obtained were processed with MaxQuant version 1.5.5.1[66] and Andromeda peak list files (.apl) generated were converted to Mascot generic files (.mgf) using APL to MGF Converter [http://www.wehi.edu.au/people/andrew-webb/1298/apl-mgf-converter.]. Generated MGF files were searched using Mascot (Matrix Science, version 2.4.1), querying dictyBase[67] (12,764 entries) plus an in-house database containing common proteomic contaminants and the sequence of GFP-NAP1. The common contaminant and reverse hits (as defined in MaxQuant output) were removed.

Mascot was searched assuming trypsin digestion allowing for two miscleavages with a fragment ion mass tolerance of 0.6 Da and a parent ion tolerance of 15 ppm. The iodoacetamide derivative of cysteine was specified in Mascot as a fixed modification, and oxidation of methionine and phosphorylation of serine, threonine and tyrosine were specified in Mascot as variable modifications. Scaffold (version 4.3.2, Proteome Software) was used to validate MS/MS based peptide and protein identifications. Peptide identifications were accepted if they could be established at greater than 95.0% probability as specified by the Peptide Prophet algorithm, resulting in a peptide false discovery rate (FDR) of 0.63%[20]. For label-free quantification, proteins were quantified according to the label-free quantification algorithm available in MaxQuant[68].

Significantly enriched proteins were selected using a Welch-test analysis with a 5% FDR.

The mass spectrometry proteomics data have been deposited to the ProteomeXchange Consortium via the PRIDE partner repository with the dataset identifier PXD010460.

Generation and Validation of *cyri*-knockout and rescued *Dictyostelium discoideum*

Primers used are detailed in Supplementary Table 5.

Standard methods were used for construction of all *Dictyostelium* knockout and re-expression vectors[69]. A linear CYRI knockout construct (2758 bp in length), which consisted of a blasticidin resistance (Bsr) cassette flanked by sequences matching 5' and 3' regions in the *CYRI* (DDB_G0272190 identifier at dictybase.org) gene locus (18pb cross-over), was made by PCR amplification using the primers set 1 (5' arm) and set 2 (3' arm). PCR-amplified arms were combined with the Bsr cassette in a using the primers set 3.

Knockout clones were screened/validated by PCR, with primers set 4. *cyri*-knockout yield a 2450 bp PCR product, random integrants (clones with a KO construct integration elsewhere in the genome) and wild-type yield a 1983 bp PCR product.

Vector for expression of untagged CYRI was obtained by sub-cloning CYRI's genomic coding region into pDM358[69]. A REMI[37] (non extra-chromosomal) vector was derived from this by removal of the *Dictyostelium* plasmid propagation genes and re-ligation of the vector backbone. This construct, while still having a strong promoter, is expected to be present in just one copy per cell.

Transformation of *Dictyostelium discoideum*

3.0 x 10^7 cells/transformation were first centrifuged (3 min, 330 x *g*, 4°C), washed with 10 ml ice-cold electroporation buffer (E-buffer; 10 mM sodium phosphate buffer pH 6.1, 50 mM sucrose), and resuspended in 400 µl ice-cold E-buffer. Cells were transferred into an ice-cold 0.2 cm electroporation cuvette and incubated 5 min with 0.5-1.0 µg of DNA on ice. Cells were electroporated (BTX-Harvard Apparatus ECM 399) at 500V, giving a time constant of 3-4ms. Cells were immediately transferred to HL5 medium in Petri dishes. Appropriate selection (50 µg/ml hygromycin or 10 µg/ml G418) was added the next day. For REMI transfections, 10 µg of linearized DNA and 50 U of restriction enzyme were used, in 0.4cm cuvettes with a Bio-Rad Gene Pulser II set at 1.2kV and 3µF.

Dictyostelium discoideum CYRI inclusion body purification

BL21(DE3) pLysS cells were grown to OD_{600nm} 0.2 and induced with 0.2 mM IPTG for 4h. Cells were pelleted, frozen and resuspended with 80 mL of lysis buffer (50 mM Tris-HCl pH 8.0, 25 % sucrose (w/v), 1 mM EDTA) per 100g of cells. Cells were lysed by adding 1% lysozyme (w/v) and kept on ice for 30 min. Lysate was resuspended with 10 mM $MgCl_2$, 1mM $MnCl_2$, 10µg/mL DNase I and kept for another 30 min on ice. Finally, 200 mL of detergent buffer (0.2 M NaCl, 1% deoxycholic acid (w/v), 1% NP40, 20 mM Tris-HCl pH 7.5, 2 mM EDTA) was added to the lysate, which is then centrifuged at 5000 x g for 10 min. Pellet is then washed in 0.5% NP40, 1 mM EDTA and this step is repeated until a tight white pellet is obtained.

Dictyostelium discoideum **CYRI antibody production**

Inclusion bodies were dissolved in sample buffer with DTT and loaded onto a 10% Bis-Tris acrylamide gel at 70V at 4 °C. Gel was Coomassie stained and fragments of the band corresponding to CYRI was sent to BioGenes for injection into 2 rabbits. Bleeds were collected every second week after initial immunisation/boost and tested by western blot.
(Terminal bleed from rabbit 27724 after 5th boost used at 1:100).

Dictyostelium discoideum **Under-agarose Chemotaxis Assay**

This assay is based on a previous study[70]. Surface of the 30 mm glass bottom dish (MatTek) was coated with 10 mg/ml BSA for 10 min, washed with dH_2O and dried for 5 min inside a laminar flow cabinet. 0.4% w/v SeaKem GTG agarose in SIH medium (Formedium) containing 10 µM folate was poured and set for 1h. A well was cut in the agarose and $2x10^6$ cells/mL placed in it. After 3-4h cells were imaged by Phase contrast and DIC microscopy with a Nikon Eclipse TE2000-E microscope system equipped with a QImaging RETIGA EXi FAST 1394 CCD camera and a pE-100 LED illumination system (CoolLED) at 525 nm. A 10×/ 0.45 NA Ph1 objective and a 60×/1.40 NA apochromatic DIC objective were used for phase contrast and DIC, respectively. Imaging was controlled through the µManager 1.4.9 software. All microscopy was carried out at RT and images were analysed with ImageJ/Fiji 1.49i.
Pseudopod rate and split frequency was analysed from the DIC movies and manually quantified frame by frame. For analysis of cell circularity, speed and migration parameters, automated tracking plugins were developed for ImageJ (see Plugin2 in Supplementary note 2). More information will be supplied upon reasonable request.

Dictyostelium discoideum **development assay**

Cells were harvested from axenic growth plates, washed twice in phosphate buffer (10 mM Na/K phosphate pH 6.5) containing 2 mM $MgCl_2$ and 1mM $CaCl_2$, and plated on 1% w/v agar prepared in the same buffer. For time-lapse imaging we used a Nikon Eclipse TE2000-E microscope fitted with a Prior ProScan II moving stage, and equipped with a QImaging RETIGA EXi FAST 1394 CCD camera and a pE-100 LED illumination system (CoolLED) at 525 nm.

cAMP needle assay

Cells were developed as described above until territories began to form, indicating production and responsiveness to cAMP waves. Cells were harvested and placed into phosphate buffer and their response to 10 µM cAMP (Eppendorf Injectman NI2 microinjector with Femtotips II) was monitored by timelapse microscopy (1 frame/5sec) using a Zeiss Axiovert A1 body with a plan/neofluar 20x 0.5NA objective combined with a QI REtiga camera.

HSPC300-GFP analysis

Wild type or *cyri* KO Ax3 cells were transfected with HSPC300-GFP as described above and timelapse movies were obtained using a Zeiss 880 confocal microscope. Processed images were used to obtain the unwrapped kymograph. Plugin used for this analysis will be provided upon reasonable request.

3D MDCK cysts - Culture

shRNA-expressing MDCK cells were split 1:10 the day before plating in 3D, in puromycin-free medium. Chilled 8-well chamber slides were coated by spreading 5 µL of undiluted Matrigel over the well surface and transferred to 37°C incubator for 10 min. MDCK cells were diluted to 4×10^4 cells/mL in puromycin-free medium and thoroughly disaggregated by pipetting. Matrigel was then diluted to 4% in MEM medium and mixed with the similar volume of cells diluted at 1.5×10^4 cells/mL, bringing the final Matrigel concentration to 2%. Wells were filled with 300 µL of the cell-Matrigel mix and cysts were grown 5 days at 37°C.

3D MDCK cysts - Immunofluorescence and Imaging

Medium was aspirated and wells were quickly washed twice with PBS. Cysts were fixed using 4% PFA for 10 min, washed, and permeabilised for 10 min at RT using 0.5% Triton X100 diluted in PBS. Cells were blocked for 30 min using PFS (0.7% (w/v) fish skin gelatin in 0.025% Saponin-PBS). Primary antibodies were diluted in PFS and incubated overnight at 4°C with gentle shaking. Cysts were washed 3x in PFS at RT. Secondary antibodies, nuclear dye and Phalloidin were diluted at 1:200 in PFS and incubated for an hour at RT before further washes. Chambers were then kept sealed in 0.02% NaN_3-PBS at 4°C until analysis. Cysts were imaged using the Nikon A1R Z6005 confocal microscope using either a Plan Apochromat 20x/0.75 DIC N2 or a Plan Fluor 10x/0.30 DIC L/N1 objective. In order to sharpen images, factor line averaging was set up at 4. Z-stack images were acquired with a 4 µm increment step from the bottom to the top of the cyst.

Statistics and Reproducibility

Data sets were analysed using Prism5 v5.0c and Prism7. Differences between groups were tested for normality and then analysed using the appropriate statistical test, mentioned in each figure legend. Error bars represent standard error of the mean (S.E.M) unless stated otherwise. Significance levels are given as follows: ns: $p>0.05$; * $p\leq0.05$; ** $p\leq0.01$; *** $p\leq0.001$. Cochran-Mantel-Haenszel test was generated using R software and *p*-values are mentioned when appropriate.
All experiments were repeated independently as biological repeats at least 3x, unless stated otherwise, and always gave similar trends. Individual values are available in Supplementary Table 6.

Data Availability

Mass spectrometry data have been deposited in ProteomeXchange with the primary accession code PXD 010460. Source data for Figs 1-7 and Supplementary Figs 2-6 have been provided as Supplementary Table 6. All other data supporting the findings of this study are available from the corresponding authors on reasonable request.

Code Availability

The code used for analysis of cell protrusions in Figure 5 is available in Supplementary Note 1. The code used for tracking *Dictyostelium* migration under agarose is available in Supplementary Note 2. Homemade plugins from this study will be made available from the corresponding authors upon reasonable request.

References

54. Kollmar, M., Lbik, D. & Enge, S. Evolution of the eukaryotic ARP2/3 activators of the WASP family: WASP, WAVE, WASH, and WHAMM, and the proposed new family members WAWH and WAML. *BMC Res Notes* **5**, 88 (2012).
55. Wheeler, T.J., Clements, J. & Finn, R.D. Skylign: a tool for creating informative, interactive logos representing sequence alignments and profile hidden Markov models. *BMC Bioinformatics* **15**, 7 (2014).
56. Kelley, L.A. & Sternberg, M.J. Protein structure prediction on the Web: a case study using the Phyre server. *Nat Protoc* **4**, 363-371 (2009).
57. Greaves, J. *et al.* Molecular basis of fatty acid selectivity in the zDHHC family of S-acyltransferases revealed by click chemistry. *Proc Natl Acad Sci U S A* **114**, E1365-E1374 (2017).
58. Vojtek, A.B. & Hollenberg, S.M. Ras-Raf interaction: two-hybrid analysis. *Methods Enzymol* **255**, 331-342 (1995).
59. Bartel, P., Chien, C.T., Sternglanz, R. & Fields, S. Elimination of false positives that arise in using the two-hybrid system. *Biotechniques* **14**, 920-924 (1993).
60. Fromont-Racine, M., Rain, J.C. & Legrain, P. Toward a functional analysis of the yeast genome through exhaustive two-hybrid screens. *Nat Genet* **16**, 277-282 (1997).
61. Ran, F.A. *et al.* Genome engineering using the CRISPR-Cas9 system. *Nat Protoc* **8**, 2281-2308 (2013).
62. Martin, K.J. *et al.* Accepting from the best donor; analysis of long-lifetime donor fluorescent protein pairings to optimise dynamic FLIM-based FRET experiments. *PLoS One* **13**, e0183585 (2018).
63. Schneider, C.A., Rasband, W.S. & Eliceiri, K.W. NIH Image to ImageJ: 25 years of image analysis. *Nat Methods* **9**, 671-675 (2012).
64. Ibarra, N., Blagg, S.L., Vazquez, F. & Insall, R.H. Nap1 regulates Dictyostelium cell motility and adhesion through SCAR-dependent and -independent pathways. *Curr Biol* **16**, 717-722 (2006).
65. McGarry, D.J., Shchepinova, M.M., Lilla, S., Hartley, R.C. & Olson, M.F. A Cell-Permeable Biscyclooctyne As a Novel Probe for the Identification of Protein Sulfenic Acids. *ACS Chem Biol* **11**, 3300-3304 (2016).

66. Cox, J. & Mann, M. MaxQuant enables high peptide identification rates, individualized p.p.b.-range mass accuracies and proteome-wide protein quantification. *Nat Biotechnol* **26**, 1367-1372 (2008).
67. Fey, P., Dodson, R.J., Basu, S. & Chisholm, R.L. One stop shop for everything Dictyostelium: dictyBase and the Dicty Stock Center in 2012. *Methods Mol Biol* **983**, 59-92 (2013).
68. Keller, A., Nesvizhskii, A.I., Kolker, E. & Aebersold, R. Empirical statistical model to estimate the accuracy of peptide identifications made by MS/MS and database search. *Anal Chem* **74**, 5383-5392 (2002).
69. Veltman, D.M., Akar, G., Bosgraaf, L. & Van Haastert, P.J. A new set of small, extrachromosomal expression vectors for Dictyostelium discoideum. *Plasmid* **61**, 110-118 (2009).

70. Woznica, D. & Knecht, D.A. Under-agarose chemotaxis of Dictyostelium discoideum. *Methods Mol Biol* **346**, 311-325 (2006).